Pixel super-resolution using spatially-entangled photon pairs

Hugo Defienne [1,*], Patrick Cameron [1], Bienvenu Ndagano [1], Ashley Lyons [1], Matthew Reichert [3], Jiuxuan Zhao [2], Edoardo Charbon [2], Jason W. Fleischer [3], and Daniele Faccio [1,†]

[1] *School of Physics and Astronomy, University of Glasgow, Glasgow G12 8QQ, UK*
[2] *Advanced Quantum Architecture Laboratory (AQUA), Ecole Polytechnique Federale de Lausanne (EPFL), 2002 Neuchatel, Switzerland*
[3] *Department of Electrical and Computer Engineering, Princeton University, Princeton, USA*

(Dated: May 24, 2021)

Pixelation occurs in many imaging systems and limits the spatial resolution of the acquired images. This effect is notably present in quantum imaging experiments with photon pairs, in which the number of pixels used to detect coincidences is often limited by the sensor technology or the acquisition speed. Here, we introduce a pixel super-resolution technique based on measuring the full spatially-resolved joint probability distribution (JPD) of spatially-entangled photon pairs. Without shifting optical elements or using prior information, our technique doubles the pixel resolution of the imaging system and enables retrieval of spatial information lost due to undersampling. We demonstrate its use in various quantum imaging protocols, including quantum illumination, entanglement-enabled quantum holography, and in a full-field version of N00N-state quantum holography. Our JPD super-resolution technique will benefit any full-field imaging system limited by the sensor spatial resolution, including all already established and future photon-pairs-based quantum imaging schemes, bringing these techniques closer to real-world applications.

Acquiring high-resolution images over a large field of view is essential in most optical imaging applications. In this respect, the widespread development of digital cameras made of millions of pixels has strongly contributed to create imaging systems with large space-bandwidth products. In classical imaging, it is therefore mainly the imaging systems with strong spatial constraints that suffer from pixelation and undersampling, such as lensless on-chip microscopes [1, 2]. However, this effect is very present in quantum imaging schemes where it severely hinders the progress of these techniques towards practical applications.

Quantum imaging systems harness quantum properties of light and their interaction with the environment to go beyond the limit of classical imaging or to implement unique imaging modalities [3]. Of the many approaches, imaging schemes based on entangled photon pairs have turned out to be among the most promising. Proof-of-principle demonstrations range from improving optical resolution [4, 5] and imaging sensitivity [6–8] to the creation of new imaging protocols, such as ghost imaging [9, 10], quantum illumination [11–13] and quantum holography [14, 15]. Contrary to classical imaging, photon-pairs-based imaging systems operate by measuring photon coincidences between many spatial positions of the image plane in parallel (except from induced-coherence imaging approaches [16–18]). In practice, this process is much more delicate than forming an intensity image by photon accumulation and therefore requires specific photodetection devices. Although such a task was originally performed with raster-scanning single-photon detectors [9], today most implementations use single-photon sensitive cameras such as electron multiplied charge coupled devices (EMCCD) [19, 20], intensified complementary metal-oxide-semiconductor (iCMOS) [21] and single-photon avalanche diode (SPAD) cameras [22].

EMCCD cameras are the most widely used devices for imaging photon-pair correlations thanks to their high quantum efficiency, low noise and high pixel resolution. However, these cameras suffer from a very low frame rate (∼100 fps) due to their electronic amplification process operating in series and therefore require very long acquisition times (∼10 hours) to reconstruct correlation images [12, 13, 15, 23]. Using a smaller sensor area or a binning technique can reduce the acquisition time, but at the cost of a loss in pixel resolution. By using an image intensifier, iCMOS cameras do not use such slow electronic amplification processes and can therefore reach higher frame rates (∼1000 fps). However, so far these cameras have only enabled correlation images with relatively small number of pixels (and still several hours of acquisition), mostly because of their low detection efficiency and higher noise level [21, 24]. Finally, SPAD cameras are an emerging technology that can detect single photons at low noise while operating at very high frame rate (up to 800 kfps). However, most devices available on the market are not yet suitable for photon pair imaging because of their low quantum efficiency (∼20%), low fill factor (∼50%) and small resolution (∼1000 pixels). For example, the commercial SPAD camera that currently has the highest pixel resolution only has 32×64 pixels (MicroPhotonDevice) [25].

It is clear from the above analysis that nearly all sensor technologies currently used in photon-pairs-based

Corresponding author:
* hugo.defienne@glasgow.ac.uk
† daniele.faccio@glasgow.ac.uk

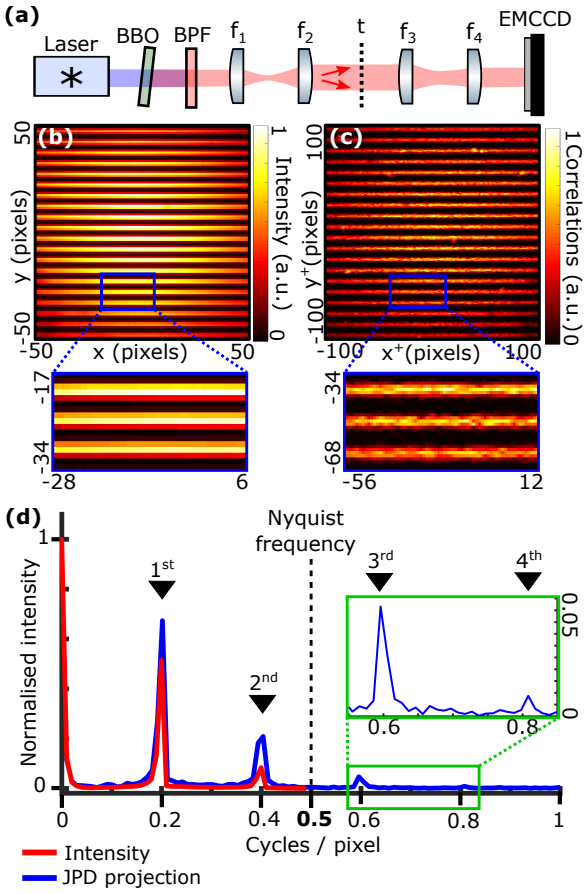

Figure 1. **Experimental results of JPD pixel super-resolution.** **(a)** Experimental setup. Light emitted by a diode laser (405 nm) illuminates β-barium borate (BBO) crystal with a thickness of 0.5 mm to produce spatially-entangled pairs of photons by type I SPDC. Long-pass and band-pass filters at 810 $\pm$ 5nm (BPF) positioned after the crystal remove pump photons. A two-lens system $f_1 - f_2$ images the crystal surface onto an object t, that is itself imaged onto the EMCCD camera by another two-lens system $f_3 - f_4$. t is a grid-shaped amplitude object with a five-pixel period. **(b)** Intensity image. **(c)** Sum-coordinate projection of the JPD $P_+(\mathbf{r}^+)$ after filtering. **(d)**. Spatial frequency spectrum of the intensity image (red curve) and sum-coordinate projection (blue curve) obtained by a discrete Fourier transform and averaging aver the x-axis. Spectral curves (blue and red) are normalised to the intensity of their respective zero-order peak. 5.10^6 frames were acquired to retrieve (b,c) in approximately 13 hours of acquisition.

imaging experiments suffer from a poor pixel resolution, either directly when the technology does not have cameras with enough pixels or indirectly when the experiment can only operate in a reasonable time with a small number of pixels. In these systems, objects are therefore often undersampled, resulting a loss of spatial information and the creation of artefacts in the retrieved images. Here, we demonstrate a quantum image processing technique that doubles the pixel resolution of any imaging sensor used in photon-pairs-based imaging schemes. Our technique harnesses the large dimensionality of the measured spatial joint probability distribution (JPD) of photon pairs to reconstruct correlation images composed of twice as many pixels as the camera used to measure it. We demonstrate the method in three common photon-pairs-based imaging schemes: two quantum illumination protocols using (i) a near-field illumination configuration with an EMCCD camera [12] and a (ii) far-field configuration with a SPAD camera [26], and (iii) one entanglement-enabled holography system [15]. In addition, we use our JPD pixel super-resolution method in (iv) a full-field version of N00N-state quantum holography, a scheme that has only been demonstrated so far using a scanning approach [6]. Note that we refer to our technique as 'pixel super-resolution' to avoid confusion with the term 'super-resolution' describing imaging techniques capable of overcoming the classical diffraction limit.

JPD pixel super-resolution technique. Figure 1.a describes the experimental setup used to demonstrate the principle of our technique. In this scheme, spatially entangled photon pairs produced by type-I SPDC in a thin β-barium Borate (BBO) crystal illuminate an object t using a near-field illumination configuration (i.e. the output surface of the crystal is imaged onto the object). The object is then imaged onto an EMCCD camera. In our experiment, t is a horizontal square-modulation amplitude grating. The recorded intensity image is shown in Figure 1.b. In the zoomed area, it is clear that the image is pixelated. This pixelation results in a loss of object spatial information, confirmed when analysing the spatial spectrum of the image (Figure 1.d, red curve). The spectrum shows only the first two harmonics at 0.2 cycles/pixel and 0.4 cycles/pixel; all harmonics higher than the Nyquist frequency of 0.5 cycles/pixel are not resolved, and their associated information is lost.

Using an EMCCD camera, one can also measure the spatially-resolved JPD of photon pairs $\Gamma(\mathbf{r_1}, \mathbf{r_2})$ by identifying photon coincidences between any arbitrary pair of pixels $\mathbf{r_1}$ and $\mathbf{r_2}$ using a method described in [27]. In practice, the information contained in the JPD can be used for various purposes. For example, it was used in pioneering works with EMCCD cameras to estimate position and momentum correlation widths of entangled photons pairs in direct imaging of the Einstein-Podolsky-Rosen paradox [19, 20]. In the experiment here, displaying the diagonal component of the JPD, $\Gamma(\mathbf{r}, \mathbf{r})$, reconstructs an image of the object. Indeed, assuming an ideal imaging system and near-perfect spatial correlations between photons [28], the JPD can be approximated as $\Gamma(\mathbf{r_1}, \mathbf{r_2}) = |t(\mathbf{r_1})t(\mathbf{r_2})\delta(\mathbf{r_1} - \mathbf{r_2})|^2$ (where δ is a Dirac delta function), resulting in a diagonal image proportional to the object shape i.e. $\Gamma(\mathbf{r}, \mathbf{r}) = |t(\mathbf{r})|^4$. Such a diagonal image is the quantity that is conventionally measured and used in all photon-pairs-based imaging schemes using a near-field illumination configuration [5, 12, 23, 29]

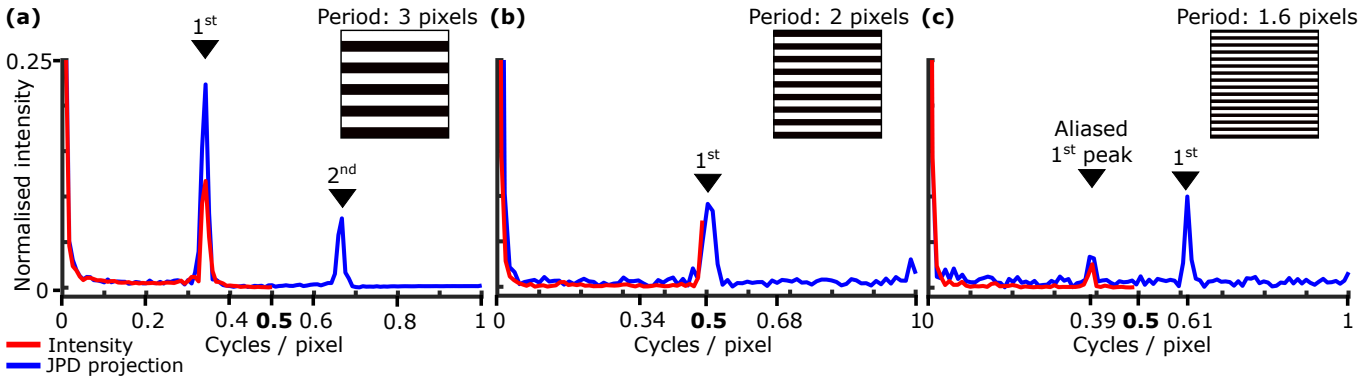

Figure 2. **Spatial frequency analysis of images of a square-wave amplitude grating with different periods,** produced using a spatial light modulator (SLM) operating in amplitude modulation (graings shown in insets). The spatial frequency spectrum of the intensity (red curves) and sum-coordinate projection (blue curve) images of gratings are shown, with periods of **(a)** 3 pixels, **(b)** 2 pixels and **(c)** 1.6 pixels. Each spectrum is obtained by performing a discrete Fourier transform and averaging aver the x-axis. All spectral curves (blue and red) are normalised to the intensity of their respective zero order peak. $2.5.10^7$ frames were acquired to retrieve intensity image and JPD in each case in approximately 20 hours of acquisition. More details in Methods.

(see section 7 of supplementary document).

Interestingly, there is another way to retrieve an image of the object without using the diagonal component of the JPD. For that, one can project the JPD along its sum-coordinate axis, achieved by integrating Γ:

$$P_+(\mathbf{r}^+) = \int \Gamma(\mathbf{r}, \mathbf{r}^+ - \mathbf{r}) d\mathbf{r} = \left| t\left(\frac{\mathbf{r}^+}{2}\right)\right|^4, \qquad (1)$$

where P_+ is defined as the sum-coordinate projection of the JPD and $\mathbf{r}^+$ is the sum-coordinate variable. Each value $P_+(\mathbf{r}^+)$ is obtained by adding all the values $\Gamma(\mathbf{r_1}, \mathbf{r_2})$ located on an anti-diagonal of the JPD defined by $\mathbf{r_1} + \mathbf{r_2} = \mathbf{r}^+$. The essential point in Eq. 1 is the presence of a scaling factor 1/2 in the spatial variable: in a discrete space, this indicates that P_+ is an image of the object sampled over twice as many points as the number of pixels of the sensor. The consequence is pixel super-resolution and the ability to retrieve lost spatial information due to undersampling.

To understand the underlying principle of our approach, it is essential to realize that the JPD is a 4D object containing much richer information than a conventional 2D intensity image. In particular, the JPD contains correlation information not only between photons detected at the same pixel on its main diagonal $\Gamma(\mathbf{r}, \mathbf{r})$, but also correlation information about photons detected between nearest-neighbour pixels on the 8 other diagonals directly above and bellow the main diagonal i.e. $\Gamma(\mathbf{r}, \mathbf{r} \pm \mathbf{e_x})$, $\Gamma(\mathbf{r}, \mathbf{r} \pm \mathbf{e_y})$ and $\Gamma(\mathbf{r}, \mathbf{r} \pm \mathbf{e_x} \pm \mathbf{e_y})$ (where $\mathbf{e_x}$ and $\mathbf{e_y}$ are the unit pixel vectors in transverse directions x and y, respectively). The 9 total diagonals are equivalent to 9 low-resolution images acquired by shifting the sensor by half of a pixel in the two transverse directions. Using an analogy with the shift-and-add technique [30], a high-resolution image is then retrieved from the diagonals by performing the integration in Equation 1 (see section 2 of the supplementary document).

In practice, calculating directly P_+ from the the measured JPD results in an image that is dominated by noise, in which the object is not visible (see Figure 6.a in Methods). Indeed, experimentally measured JPD correlation values are noisy, and all the noise from each diagonal adds up in the integration in Equation 1, ultimately producing a noise of greater variance that dominates the signal in the final image. To solve this issue, we apply a filtering technique to the JPD to remove the weakest correlation values that have a negligible contribution in the final image. By doing so, we also remove the noise associated with these values and significantly improve the quality of the final image. This filtering technique does not require prior information of the object nor the source. After filtering, the calculated sum-coordinate projection P_+ is normalised to remove the so-called 'motion error artefact' (see Methods). In the case of the experiment in Figure 1.a, by filtering the JPD, we effectively set to zero all correlation values except those in the main diagonal and the off-centre diagonals that are kept. Figure 1.c shows the resulting sum-coordinate projection of the measured JPD after filtering. It reveals the grating amplitude with an increased pixel resolution compared to the direct intensity image. Figure 1.d shows the spatial frequency spectrum of the image projected along the x-axis (blue curve) and confirms that our approach retrieves additional spatial information content (harmonics at 0.6 cycles/pixel and 0.8 cycles/pixel) that cannot be resolved by the conventional intensity measurement.

Experimental results with different grating periods, ranging from 3 to 1.6 pixels are shown in Figures 2.a-c. These results further confirm that our technique retrieves spatial information content of an object that is not visible in the intensity image, even in the case where the first harmonic has a higher frequency than

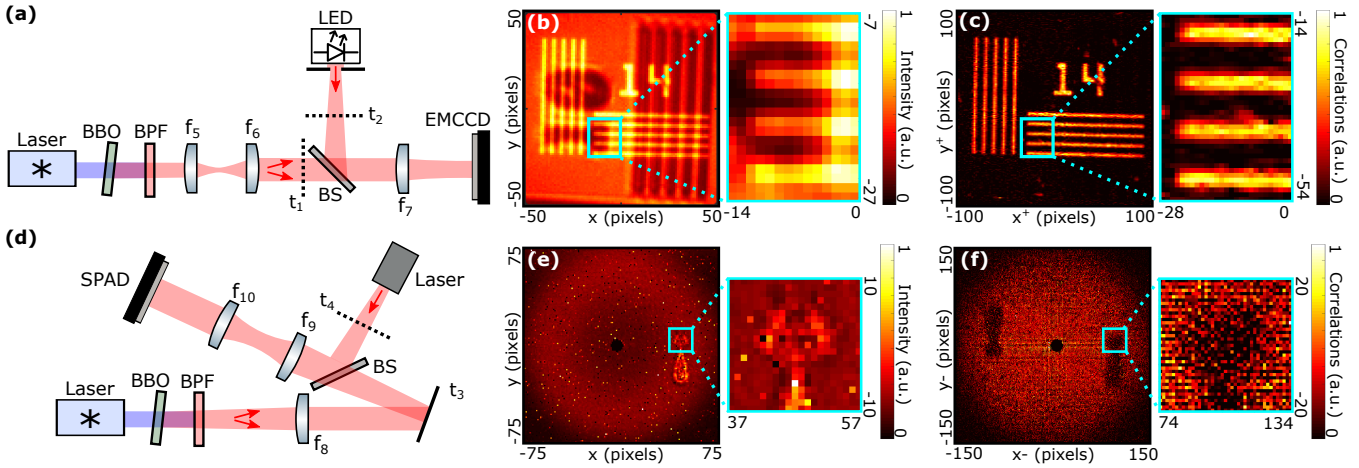

Figure 3. **Results in quantum illumination imaging**. **(a)** Experimental setup for quantum illumination in a near-field configuration. Photon pair source and the EMCCD camera are the same as those used in Figure 1.a. A two-lens system $f_5 - f_6$ images the crystal surface onto an object t_1, that is in turn imaged onto the EMCCD camera by a single-lens imaging system f_7. An object t_2 is inserted and illuminated by a spatially filtered light-emitting diode (LED) and spectrally filtered at 810 ± 5 nm. Images of both objects are superimposed on the camera using a beam splitter (BS). t_1 and t_2 are negative and positive amplitude USAF resolution charts, respectively. **(b)** Intensity image. **(c)** Sum-coordinate projection of the filtered JPD $P_+(\mathbf{r}^+)$. 6.10^6 frames were acquired to retrieve intensity image and JPD in approximately 20 hours of acquisition. **(d)** Experimental setup for quantum illumination in a far-field configuration. Light emitted by a pulsed laser (347 nm) illuminates a BBO crystal (1 mm thickness) to produce spatially entangled photon pairs (694 nm) by type-I SPDC. After the crystal, pump photons are filtered out by a BPF at 694 ± 10 nm. A lens f_8 is used to Fourier-image photon pairs onto a reflective object t_3, that is then imaged onto the SPAD camera by a two-lens system $f_9 - f_{10}$. Another laser (633 nm) illuminates an object t_4 that is also imaged onto the camera using a BS. t_3 is a cat-shape reflective object and t_4 is a transmission object with the same cat-shape, positioned so that the cat shapes overlap on the sensor. **(e)** Intensity image. **(f)** Minus-coordinate projection of the filtered JPD $P_-(\mathbf{r}^-)$. 10^7 frames were acquired to retrieve the intensity image and JPD in approximately 7.5 hours of acquisition.

the Nyquist limit of 0.5 cycles/pixel (Figure 2.c). In this latter case, we also observe the presence of an aliased frequency peak in the intensity spectrum at 0.39 cycles/pixel (red curve), which is expected when an image is undersampled. Note also that a similar peak appears at the same position in the JPD projection image (blue curve), that is however not predicted by Equation 1. This small residual frequency peak (25% of the first harmonic at 0.61 cycles/pixel) is an artefact originating from imperfections in the JPD measured with an EMCCD camera [27] (see Methods). The experimental results obtained in Figure 1 and 2 are in very good accordance with simulations (see section 3 of supplementary document).

Applications to quantum illumination. We demonstrate our technique on two different experimental schemes based on quantum illumination protocols described in [12] and [26]. In the first implementation (Figure 3.a), an amplitude object t_1 is illuminated by photon pairs and imaged onto an EMCCD camera using a near-field imaging configuration. Simultaneously, another object t_2 is illuminated by a classical source and also imaged on the camera. The intensity image, Figure 3.b, shows a superposition of both quantum and classical images. The goal of this protocol is to segment the quantum object and therefore retrieve an image showing only object t_1 illuminated by photon pairs, effectively removing any classical objects or noise. Using our image processing method, we achieve such a task and simultaneously retrieve a pixel super-resolved image of t_1 (Figure 3.d).

In the second quantum illumination protocol, an object t_3 (a reflective amplitude object) is illuminated using a far-field configuration and its image is measured with a SPAD camera (Figure 3.d). Another object t_4 (a transmission object with the same shape as t_3) is illuminated by a classical source and also imaged on the SPAD camera. Objects are positioned so that they overlap exactly on the camera, as shown in the intensity image in Figure 3.e. In such a far-field configuration, it is important to understand that information of the JPD is concentrated around the anti-diagonal because photon pairs are spatially anti-correlated in the object plane [31]. Consequently, an image of t_3 can then be retrieved by displaying the main anti-diagonal component $\Gamma(\mathbf{r}, -\mathbf{r})$. Such an anti-diagonal image is the quantity that is conventionally measured and used in all photon-pairs-based imaging schemes using a far-field illumination configuration [13, 15, 26] (see section 7 of supplementary document). In this case, the JPD pixel super-resolution technique must be adapted by using the minus-coordinate

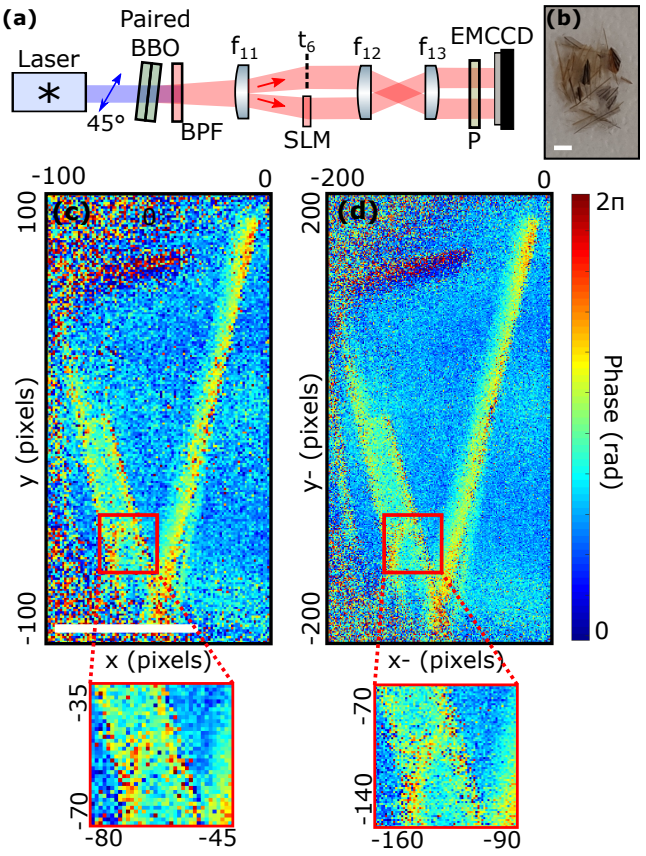

Figure 4. **Results in entanglement-enabled quantum holography.(a)** Experimental setup. Light emitted by a laser diode at 405 nm and polarized at 45° illuminates a stacked BBO crystal pair (0.5 mm thickness each) whose optical axes are perpendicular to each other to produce pairs of photons entangled in space and polarization by type-I SPDC. After the crystals, pump photons are filtered out by a band pass filter at 810 ± 5nm. A lens f_{11} is used to Fourier-image photon pairs onto an optical plane where an SLM with a phase object t_6. A two-lens imaging system $f_{12} - f_{13}$ is then used to image the SLM and the object onto two different parts of an EMCCD camera. A polarizer (P) at 45° is positioned before the camera. **(b)** Photo of the birefringent object used in the experiment (section of a bird feather). **(c)** Spatial phase of the object reconstructed by combining four anti-diagonal images $\Gamma(\mathbf{r}, -\mathbf{r})$ measured for four phase shifts $\{0, \pi/2, \pi/2, 3\pi/4\}$ programmed by the SLM. **(d)** Spatial phase of the same object reconstructed from four minus-coordinate projections $P_-(\mathbf{r}^-)$. $2.5.10^6$ frames were acquired to retrieve intensity image and JPD in each case in approximately 17 hours of acquisition. White scale bar is 1 mm.

projection P_- of the filtered JPD in place of the sum-coordinate projection P_+ to retrieve the high-resolution image (Figure 3.f). Even though this image has a better pixel resolution, we also observe that it has a lower signal-to-noise ratio (SNR) and the presence some horizontal dark stripe artefacts. These effects are due to the poor quantum efficiency (2.6%) and fill-factor (10.5%) of the SPAD camera. In addition, note that the object appears twice in the image (the vertical cat-shape and its rotated symmetric copy), which is a known consequence of using a far-field illumination configuration [15, 26] (see Methods).

Application to quantum holography. We now demonstrate our technique on two different experimental quantum holography schemes. The first protocol under consideration was demonstrated in [15] and its experimental configuration is described in Figure 4.a. Pairs of photons entangled in space and polarisation illuminate an SLM and a birefringent phase object t_6 positioned in each half of an optical plane using a far-field illumination configuration. The object and SLM are then both imaged onto two different parts of an EMCCD camera. The object is a section of a bird feather (Fig. 4.b). The SLM is used to compensate for optical aberrations and implement a four phase-shifting holographic process by displaying uniform phase patterns with values $\{0, \pi/2, \pi, 3\pi/2\}$ (see Methods). In the original protocol, four different images are obtained for each step of the process by measuring the anti-diagonal component $\Gamma(\mathbf{r}, -\mathbf{r})$ of the JPD. These images are then combined numerically to reconstruct the spatial phase of the birefringent object (Figure 4.c). Using our new JPD pixel super-resolution approach, the four images are now obtained from the minus-coordinate projection of the JPD and recombined to retrieve a phase image with improved spatial resolution (Figure 4.d).

The second protocol is a full-field version of a N00N-state holographic scheme based on photon pairs (N=2) [6]. N00N states provide phase measurements with N-times better sensitivity than classical holography [7]. As shown in Figure 5, photon pairs entangled in space and polarisation pass through an SLM and illuminate a birefringent object t_7. In this case, we use a near-field configuration and the object, SLM and EMCCD camera are all positioned in conjugate image planes. In our experiment, t_7 is a checkerboard birefringent phase pattern composed of 9 square areas with different phase values (Figure 5.b). The SLM is used to perform a phase-shifting holographic process at four phase values $\{0, \pi/4, \pi/2, 3\pi/4\}$. Sum-coordinate projections of four filtered JPDs are measured at each step of the process and then combined to reconstruct the object phase image (see Methods) shown in Figure 5.c. This image has better pixel resolution than the phase image of the same object retrieved using an equivalent classical holographic system, shown in Figure 5.d. Furthermore, it is worth noting that phase values in the image retrieved using photon pairs are twice those of the object and the classical phase image, as expected for N00N-state holography and also as demonstrated in previous scanning-based imaging approach with N00N states [6, 7]. In addition to preserving this sensitivity enhancement, our full-field version of N00N-state holography then also provides a better pixel resolution, an advantage that could only be matched with the

scanning version by increasing the acquisition time by at least a factor of four. The range of applications can be extended to non-birefringent phase objects by using birefringent plates, as done in differential interference contrast microscopy [32, 33].

Conclusion. We have introduced a pixel super-resolution technique based on the measurement of a spatially-resolved JPD of spatially-entangled photon pairs. This approach retrieves spatial information about an object that is lost due to pixelation, without shifting optical elements or relying on prior knowledge. We demonstrated that this JPD pixel super-resolution approach can improve the spatial resolution in already established quantum illumination and entanglement-enabled holography schemes, as well as in a full-field version of N00N-state quantum holography, using different types of illumination (near-field and far-field) and different single-photon-sensitive cameras (EMCCD and SPAD). Our approach has the advantage that it can be used immediately in quantum imaging schemes based on photon pairs, and even in some cases by only reprocessing already acquired data. In addition, our approach can also be implemented in any classical imaging system limited by pixelation, after substituting the classical source by a source of entangled photon pairs with similar properties. Indeed, contrary to classical pixel super-resolution techniques, such as shift-and-add approaches [30], wavelength scanning [34] and machine-learning-based algorithms [35], our JPD super-resolution approach has the strong advantage that it does not require displacing optical elements in the system or having prior knowledge about the object being imaged. Our JPD pixel super-resolution approach can therefore benefit all quantum and classical imaging applications in which the spatial resolution is limited by the camera pixel size.

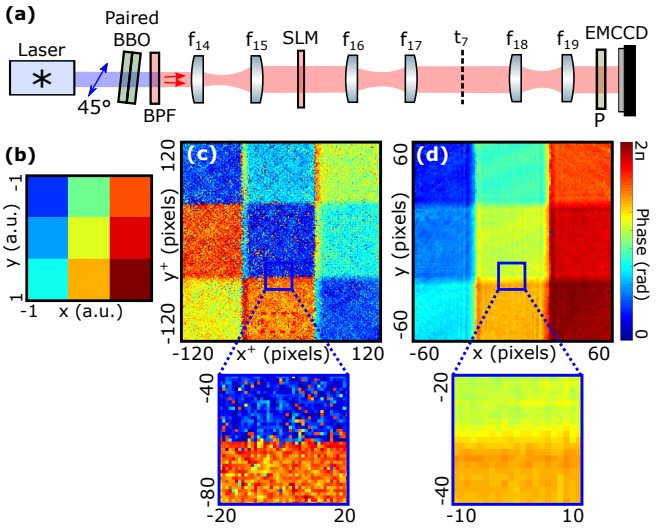

Figure 5. **Results in full-field N00N-state quantum holography. (a)** Experimental setup. Pairs of photons entangled in space and polarization are produced by type I SPDC using the same source of Figure 4.a. Three consecutive two-lens systems $f_{14} - f_{15}$, $f_{17} - f_{18}$ and $f_{19} - f_{20}$ are used to successively image the crystal surface onto a SLM, an object t_7 and onto an EMCCD camera. A polarizer (P) at 45° is positioned before the camera. **(b)** The object t_7 is a checkerboard birefringent phase pattern composed of 9 squared areas with different phase values uniformly distributed in $[0, 2\pi]$ created using another SLM. **(c)** Spatial phase image obtained by combining four sum-coordinate projections $P_+(\mathbf{r}^+)$ measured for four different phase shifts $\{0, \pi/4, \pi/2, 3\pi/4\}$ programmed by the SLM. **(d)** Spatial phase of the same object reconstructed by classical holography after replacing the source of photon pairs by a laser at 810 nm and 45° polarisation and measuring four intensity images measured for four different phase shifts $\{0, \pi/2, \pi, 3\pi/2\}$. 2.10^7 frames were acquired to retrieve the JPD in each case in approximately 30 hours of acquisition.

METHODS

Experimental layouts. *Experiment in Figure 1.a:* BBO crystal has dimensions of $0.5 \times 5 \times 5$ mm and is cut for type I SPDC at 405 nm with a half opening angle of 3 degrees (Newlight Photonics). It is slightly rotated around horizontal axis to ensure near-collinear phase matching of photons at the output (i.e. ring collapsed into a disk). The pump is a continuous-wave laser at 405 nm (Coherent OBIS-LX) with an output power of approximately 200 mW and a beam diameter of 0.8 ± 0.1 mm. A 650 nm-cut-off long-pass filter is used to block pump photons after the crystals, together with a band-pass filter centred at 810 ± 5 nm. The camera is an EMCCD (Andor Ixon Ultra 897) that operates at $-60°$C, with a horizontal pixel shift readout rate of 17 MHz, a vertical pixel shift every 0.3 μs, a vertical clock amplitude voltage of +4V above the factory setting and an amplification gain set to 1000. It has a 16μm pixel pitch. Exposure time is set to 2 ms. The camera speed is about 100 frames per second (fps) using a region of interest of 100×100 pixels. The two-lens imaging system $f_1 - f_2$ in Fig. 1.a is represented by two lenses for clarity, but is composed of a series of 6 lenses with focal lengths 45 mm - 75 mm - 50 mm - 150 mm - 100 mm - 150 mm. The first and the last lens are positioned at focal distances from the crystal and the object, respectively, and the distance between two lenses in a row equals the sum of their focal lengths. Similarly, the second two-lens imaging system $f_3 - f_4$ in Figure 1.a is composed of a series of 4 consecutive lenses with focal lengths 150mm - 50 mm - 75 mm - 100 mm arranged as in the previous case.

Experiment in Figure 3.a: Laser, camera and photon-pairs source are the same than in Figure 1.a. Exposure time is set to 6 ms. The two-lens imaging system $f_5 - f_6$ is composed of two lenses with focal lengths 35 mm and 75 mm. The single-lens imaging system f_7 is composed of one lens with focal length 50 mm positioned at a distance of 100mm from both objects and the camera. The same setup was used in [12].

Experiment in Figure 3.d: BBO crystal has dimensions $5 \times 5 \times 1$mm cut for type-I SPDC at 355nm with a half opening angle of 3 degrees (Newlight Photonics). It is slightly rotated around horizontal axis to ensure near-collinear phase matching of photons at the output (i.e. ring collapsed into a disk). The pump is the third harmonic at 347 nm of a femtosecond pulsed laser with 100 MHz repetition rate, 80 mW average power and beam-diameter of approximately 0.5 mm (Chromacity). The SPAD camera is the *SwissSPAD2* [36]. It has a total of 512×512 pixels, a fill-factor of 10.5%, a photon detection efficiency of 2.6%, a pixel pitch of 16.83 μm and a frame rate of 370 fps. The Fourier-imaging system f_8 is composed of one lens with focal length 45 mm. The two-lens imaging system $f_9 - f_{10}$ is composed of two lenses with focal lengths 100 mm and 50 mm. The same setup was used in [26].

Experiment in Figure 4.a: The paired set of stacked BBO crystals have dimensions of $0.5 \times 5 \times 5$ mm each and are cut for type I SPDC at 405 nm. They are optically contacted with one crystal rotated by 90 degrees about the axis normal to the incidence face. Both crystals are slightly rotated around horizontal and vertical axis to ensure near-collinear phase matching of photons at the output (i.e. rings collapsed into disks). The pump laser and camera are the same than in Figure 1.a. A 650 nm-cut-off long-pass filter is used to block pump photons after the crystals, together with a band-pass filter centred at 810 ± 5 nm. The SLM is a phase only modulator (Holoeye Pluto-2-NIR-015) with 1920×1080 pixels and a 8 μm pixel pitch. For clarity, it is represented in transmission in Figure 4.a, but was operated in reflection. Exposure time is set to 3 ms. The camera speed is about 40 frame per second using a region of interest of 200×200 pixels. The single-lens Fourier imaging system f_{11} is composed of a series of three lenses of focal lengths 45 mm - 125 mm - 150 mm. The first and last lenses are positioned at focal distance from the crystal and the object-SLM plane, respectively, and the distance between each pair of lenses equals the sum of their focal lengths. The two-lens imaging system $f_{12} - f_{13}$ is in reality composed by a series of 4 lenses with focal lengths 150 mm - 75 mm - 75 mm - 100 mm. The first and the last lens are positioned at focal distances from respectively the SLM-object and the camera, respectively, and the distance between two lenses in a row equals the sum of their focal lengths. The same setup was used in [15] and in section 5 of the supplementary document.

Experiment in Figure 5.a: Laser, camera, SLM, filters and photon-pairs source are the same than in Figure 4.a. The two-lens imaging system $f_{14} - f_{15}$ is composed of a series of 4 lenses with focal lengths 45 mm - 75 mm - 50 mm - 150 mm. They are arranged so that the first and last lenses are positioned at focal length from the crystal and the SLM, respectively, and the distance between each pair of lenses equals the sum of their focal lengths. The two-lens imaging system $f_{16} - f_{17}$ is composed of two lenses with focal lengths 100 mm and 150 mm. Similarly, the second two-lens imaging system $f_{18} - f_{19}$ in Figure 1.a is in reality composed of a series of 4 lenses with focal lengths 150mm - 50 mm - 75 mm - 100 mm, arranged as for $f_{14} - f_{15}$. More details in section 6 of the supplementary document.

JPD measurement with a camera. $\Gamma(\mathbf{r_1}, \mathbf{r_2})$, where $\mathbf{r_1}$ and $\mathbf{r_2}$ are positions of camera pixels, is measured by acquiring a set of $N+1$ frames $\{I_l\}_{l \in [\![1, N+1]\!]}$ using a fixed exposure time and then processing them using the formula:

$$\Gamma(\mathbf{r_1}, \mathbf{r_2}) = \frac{1}{N} \sum_{l=1}^{N} [I_l(\mathbf{r_1}) I_l(\mathbf{r_2}) - I_l(\mathbf{r_1}) I_{l+1}(\mathbf{r_2})] \quad (2)$$

In all the results of our work, N was on the order of $10^6 - 10^7$ frames. However, it is essential to note

that not all the JPD values can be directly measured using this process. When using an EMCCD camera, (i) correlation values at the same pixel, i.e. $\Gamma(\mathbf{r},\mathbf{r})$, cannot be directly measured because Equation 2 is only valid for different pixels $\mathbf{r_1} \neq \mathbf{r_2}$ [27], and (ii) and correlation values between vertical pixels, i.e. $\Gamma(\mathbf{r},\mathbf{r} \pm k_y\mathbf{e_y})$ (where k_y is an integer that defines the position of a pixel above or bellow $\mathbf{r}$), cannot be measured because of the presence of charge smearing effects. To circumvent this issue in practice, these values are interpolated from neighbouring correlation values of the JPD i.e. $[\Gamma(\mathbf{r},\mathbf{r}+\mathbf{e_x})+\Gamma(\mathbf{r},\mathbf{r}-\mathbf{e_x})]/2 \rightarrow \Gamma(\mathbf{r},\mathbf{r})$ and $[\Gamma(\mathbf{r},\mathbf{r} \pm k_y\mathbf{e_y}+\mathbf{e_x})+\Gamma(\mathbf{r},\mathbf{r} \pm k_y\mathbf{e_y}-\mathbf{e_x})]/2 \rightarrow \Gamma(\mathbf{r},\mathbf{r} \pm k_y\mathbf{e_y})$, as detailed in [5]. As a result, the gain in resolution along the x-axis in the experiments using near-field imaging configurations (Figure 1.a, 3.a, 6.a) is not optimal. However, it is important to note that the gain in pixel resolution along the y-axis is not affected by this interpolation technique. Therefore, the spectral analyses performed in Figures 1 and 2 are also not impacted because the grid-objects used are horizontal (no spectral component on the x-axis) and all the resulting spectral curves are obtained by summing along the x-axis. In addition, this interpolation also does not affect experiments using far-field illumination configurations in Figures 3.d and 5.a because the JPD diagonals do not contain any relevant imaging information (that is in the JPD anti-diagonals). More details are provided in [27] and in section 1 of the supplementary document.

JPD pixel super-resolution in far-field illumination configuration. When an object is illuminated by photon-pairs using a far-field illumination configuration (i.e. the crystal is Fourier-imaged on the object), the JPD super-resolution technique must be adapted and the sum-coordinate projection P_+ cannot be used to retrieve the high-resolution image. Indeed, assuming an ideal imaging system and near-perfect spatial correlations between photon pairs [28], the JPD measured by the camera using a far-field illumination configuration can be written as:

$$\Gamma(\mathbf{r_1},\mathbf{r_2}) = \left|t(\mathbf{r_1})t(\mathbf{r_2})\delta(\mathbf{r_1}+\mathbf{r_2})\right|^2, \quad (3)$$

where δ is a Dirac delta function. Information about the object can then be retrieved by displaying the anti-diagonal component of the JPD i.e. $\Gamma(\mathbf{r},-\mathbf{r}) = |t(\mathbf{r})|^2|t(-\mathbf{r})|^2$. $\Gamma(\mathbf{r},-\mathbf{r})$ is the quantity that is conventionally measured and used in all photon-pairs-based imaging schemes using a far-field illumination configuration [13, 15, 26]. Interestingly, it is also possible to retrieve information about the object by integrating the JPD along its minus-coordinate axis:

$$P_-(\mathbf{r}^-) = \int \Gamma(\mathbf{r},\mathbf{r}+\mathbf{r}^-)d\mathbf{r} = \left|t\left(\frac{\mathbf{r}^-}{2}\right)t\left(\frac{-\mathbf{r}^-}{2}\right)\right|^2, \quad (4)$$

where P_- is defined as the minus-coordinate projection of the JPD and $\mathbf{r}^-$ is the minus-coordinate variable. Each value $P_-(\mathbf{r}^-)$ is obtained by adding all the values $\Gamma(\mathbf{r_1},\mathbf{r_2})$ located on a diagonal of the JPD defined by $\mathbf{r_1}-\mathbf{r_2}=\mathbf{r}^-$. An essential point in Eq. 4 is the presence of a scaling factor 1/2 in the spatial variable. In a discrete space, it means that P_- is an image of the object sampled over twice as many points as the number of pixels of the sensor. In theory, calculating the minus-coordinate projection of the JPD can therefore achieve pixel super-resolution and potentially retrieved lost spatial information of undersampled objects. However, it is important to note that the JPD anti-diagonal $\Gamma(\mathbf{r},-\mathbf{r})$ and minus-coordinate projection P_- images are not directly proportional to $|t(\mathbf{r})|$ as in the near-field configuration, but to $|t(\mathbf{r})||t(-\mathbf{r})|$, which does not always enable to retrieve $|t|$ without ambiguity. In works using a far-field illumination configuration, this problem is solved by illuminating t with only half of the photon pairs beam (i.e. $t(x,y \leqslant 0) = 1$). The object then appears in double in the retrieved image (object and its symmetric), but no information is lost.

JPD filtering. Figure 6.a shows the sum-coordinate projection P_- calculated using equation 1 from the unfiltered JPD measured in Figure 1.a. This image is very noisy and does not reveal the object. To solve this issue, a filtering method is applied and consists in setting to 0 all values of the JPD that have a negligible weight (i.e. values close to zero) so that their associated noise does not contribute when performing the integration. To perform this selection efficiently, correlation values with the lowest weights are not selected individually but by groups. To distinguish these groups, we must differentiate the two cases of an object illuminated by photon pairs using (i) a near-field illumination configuration (Figures 1.a, 3.a and 5.a) and (ii) a far-field configuration (Figures 3.d and 4.a).

Near-field configuration: Using a near-field illumination configuration, each group corresponds to all the correlation values located in a specific JPD diagonal $\Gamma(\mathbf{r},\mathbf{r}+\mathbf{r}^-)$, where $\mathbf{r}^-$ defines the position of the diagonal. To assess the weights of the different JPD diagonals, the minus-coordinate projection of the JPD (noted P_-) is calculated using the integration defined in Eq. 4. Each value $P_-(\mathbf{r}^-)$ is the sum of all the correlation values $\Gamma(\mathbf{r_1},\mathbf{r_2}+\mathbf{r}^-)$ located on the diagonal defined by $\mathbf{r_1}-\mathbf{r_2}=\mathbf{r}^-$ and therefore provides a direct estimation of the corresponding diagonal weight. For example, Fig. 6.b shows the minus-coordinate projection obtained using the JPD measured in the experiment of Fig. 1.a. We observe that only a small number of diagonals (values around the center in P_-) have significant weights, while all the others are almost zero. By applying a threshold, only the highest values of P_- are kept, which in the case of the experiment in Fig. 1.a corresponds to keeping values of the main JPD diagonal $\Gamma(\mathbf{r},\mathbf{r})$ (i.e. center pixel of P_-) and those of the 8 other diagonals directly above and bellow i.e. $\Gamma(\mathbf{r},\mathbf{r} \pm \mathbf{e_x})$, $\Gamma(\mathbf{r},\mathbf{r} \pm \mathbf{e_y})$ and $\Gamma(\mathbf{r},\mathbf{r} \pm \mathbf{e_x} \pm \mathbf{e_y})$ (direct-neighbour

around the center pixel in P_-). After filtering the JPD, the integration in Eq. 1 is performed and a normalisation process is used (see next Methods section) to retrieve the low-noise high-resolution image shown in Fig. 1.c.

Far-field configuration: Using a far-field illumination configuration, the process is the same as in the near-field configuration described above after inverting the roles played by the minus-coordinate P_- and sum-coordinate P_+ projections. In this configuration, the JPD sum-coordinate projection P_+ enables to assess the weights of the different group of correlations values associated with specific JPD anti-diagonals. For example, Figure 6.c shows P_+ measured using the experiment in Figure 4.a, in which a peak of correlation is well visible. By applying a threshold on this image, only the highest values of P_+ are kept (i.e. those in the correlation peak), which corresponds to keeping values of the main JPD anti-diagonal $\Gamma(\mathbf{r}, -\mathbf{r})$ (i.e. pixel at the center of the peak) and those of the 8 other anti-diagonals directly above and bellow i.e. $\Gamma(\mathbf{r}, -\mathbf{r} \pm \mathbf{e_x})$, $\Gamma(\mathbf{r}, -\mathbf{r} \pm \mathbf{e_y})$ and $\Gamma(\mathbf{r}, \mathbf{r} \pm \mathbf{e_x} \pm \mathbf{e_y})$ (i.e. pixel surrounding the center of the peak). After filtering the JPD, the integration in Eq. 4 is performed and a normalisation process is used (see next Methods section) to retrieve a low-noise high-resolution image.

Symmetric roles of P_+ and P_-: We underline that both the sum-coordinate P_+ and minus-coordinate P_- projections of the JPD are used in both near-field and far-field configurations, but their roles are different. In a near-field configuration, P_- is first calculated from the measured JPD to apply the filtering process, and then P_+ is calculated to retrieve the high-resolution image from the filtered JPD. In a far-field configuration, P_+ is first calculated from the measured JPD to apply the filtering process, and then P_- is calculated to retrieve the high-resolution image from the filtered JPD. More details are provided section 4 of the supplementary document.

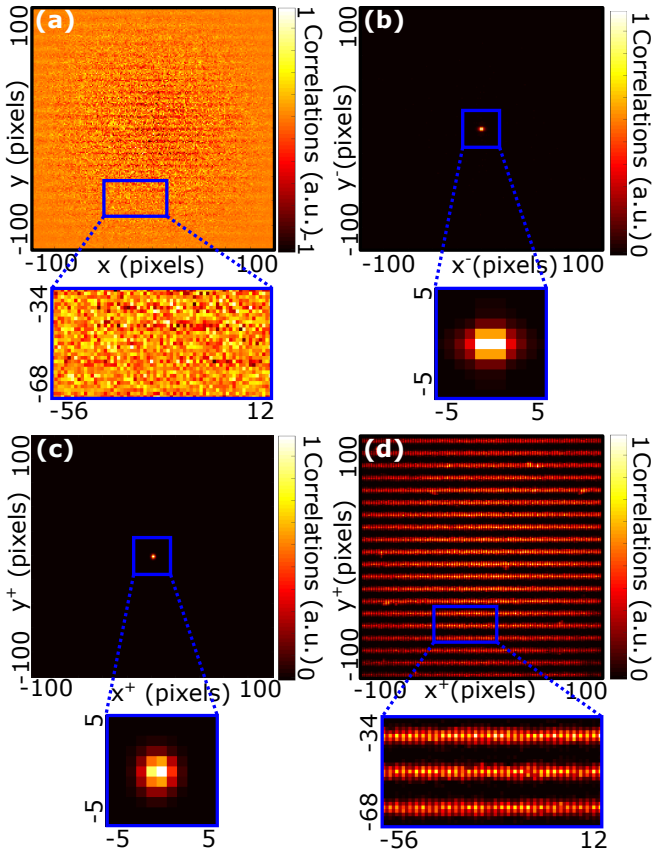

Figure 6. **(a)** Sum-coordinate projection of the JPD $P_+(\mathbf{r}^+)$ measured in the experiment in Figure 1.a without filtering. **(b)** Minus-coordinate projection image of the JPD $P_-(\mathbf{r}^-)$ measured in the experiment in Figure 1.a without filtering. **(c)** Sum-coordinate projection of the JPD $P_+(\mathbf{r}^+)$ measured in the experiment in Figure 4.a without filtering. **(d)** Sum-coordinate projection of the JPD $P_+(\mathbf{r}^+)$ measured in the experiment in Figure 1.a after filtering and before normalisation.

Normalisation. Figure 6.d shows the sum-coordinate projection P_+ directly calculated from the filtered JPD measured in the experiment in Figure 1.a. We observe that this image has an artefact taking the form of inhomogeneous horizontal and vertical stripes. This artefact is very similar to this commonly observed in shift-and-add super-resolution techniques [30] and is often refereed as a 'motion error artefact'. In our case, it originates from the approximation made when substituting the integration in Equation 1 by a summation in a discrete space to calculate P_+, and also from the JPD filtering. Using an analogy with the shift-and-add technique, our problem is equivalent to a situation in which the different shifted low-resolution images were measured using sources with different averaged intensity during the first step of the process. Then, when these low-resolution images are recombined into a high-resolution one (second step of shift-and-add), the artefact appears in the resulting image because some pixels placed next to each others were not acquired using the same intensity. In practice, the most basic way to remove this artefact is to normalise each low-resolution image by its total average intensity, so that neighbouring pixels in the high-resolution image are at the same level. We use such a normalisation approach in our work by dividing all values of the non-zero diagonals in the filtered JPD by their spatial average value i.e. $\Gamma(\mathbf{r}, \mathbf{r}+\mathbf{r}^-) \rightarrow \Gamma(\mathbf{r}, \mathbf{r}+\mathbf{r}^-)/\sum_{\mathbf{r}} \Gamma(\mathbf{r}, \mathbf{r}+\mathbf{r}^-)$, where $\mathbf{r}^-$ identifies a specific JPD diagonal. After normalisation, Figure 1.c is obtained. In the case of far-field illumination, the same normalisation is applied to the values of the non-zero anti-diagonals in the filtered JPD i.e. $\Gamma(\mathbf{r}, -\mathbf{r}+\mathbf{r}^+) \rightarrow \Gamma(\mathbf{r}, -\mathbf{r}+\mathbf{r}^+)/\sum_{\mathbf{r}} \Gamma(\mathbf{r}, -\mathbf{r}+\mathbf{r}^+)$, where $\mathbf{r}^+$ identifies a specific JPD anti-diagonal.

In some cases, such as in Fig. 4.f, the artefact is reduced but still visible in the resulting image even after normalisation. The persistence of this artefact is due the fact that the anti-diagonals are not only different in

terms of their average intensity (that can be corrected by normalisation), but they are also different in terms of their spatial shape. By analogy to shift-and-add, a similar artefact would be present if the different shifted low-resolution images were measured using sources of light with different distribution of spatial intensity. In the experiment shown in Figure 4.d, the difference in spatial shape of the JPD anti-diagonals originates from the poor quality of the SPAD camera sensor, in particular from its very low fill-factor (10.5%), that can create spatial inhomogeneities in the coincidence values measured for different pair of pixels depending on how the sensor is positioned relative to the source and the object. To further reduce this artefact, one could use more complex normalisation algorithms, such as L_1 or L_2 norms minimisation approaches [37] and kernel regression [38], that are commonly used in shift-and-add.

Full-field N00N-state quantum holography. In the holographic process used in full-field N00N-state holography (Fig. 5.a), different JPDs are measured for different uniform phase values programmed on the SLM. For each phase value α, the sum-coordinate projection of the JPD (noted P_+^α) is proportional to $1+\cos(2\Delta\theta-2\alpha)$, where $\Delta\theta = \theta_H - \theta_V$ with θ_H (resp. θ_V) the horizontal (resp. vertical) phase component of t_7. To reconstruct the phase image (Figure 5.c), JPD projections measured for four phases $\alpha \in \{0, \pi/4, \pi/2, 3\pi/4\}$ are recombined using the formula: $\arg[P_+^0 - P_+^{\pi/2} + i(P_+^{\pi/4} - P_+^{3\pi/4})] = 2\Delta\theta$. To retrieve the classical phase image (Fig. 5.d), the photon pair source is first substituted by a collimated laser beam at 810nm and polarized at 45°. Then, as conventionally done in quantitative phase imaging [39], four intensity images (noted I^α) are measured for four different constant phase value programmed on the SLM $\alpha \in \{0, \pi/2, \pi, 3\pi/2\}$ and combined using the formula $\arg[I^0 - I^\pi + i(I^{\pi/2} - I^{3\pi/2})] = \Delta\theta$ to retrieve the spatial phase of the object θ. More details are provided section 6 of the supplementary document, including images of JPD projections measured for each phase value and a description of the equivalent classical holography experiment used to retrieved the phase image shown in Fig. 5.d

Residual aliased peak in the JPD projection. As detailed in [27], the use of Eq. 2 to measure the JPD with an EMCCD camera is not perfect and a residual background $\mathcal{B}$ is also retrieved i.e. $\Gamma(\mathbf{r_1}, \mathbf{r_2}) + \mathcal{B}$. This background originates from the fluctuations of the EMCCD camera gain during the acquisition process. $\mathcal{B}$ is proportional to $\alpha I(\mathbf{r_1})I(\mathbf{r_2}) + \beta(I(\mathbf{r_1}) + I(\mathbf{r_2})) + \gamma$, where α, β and γ are constant experimental parameters, and $I(\mathbf{r})$ is the intensity value at pixel $\mathbf{r}$. In most experiments, $\mathcal{B}$ is negligible compared to Γ and is just ignored. However, when performing the experiment with a high-frequency grid-shaped object of period 1.6 pixels (Fig. 2.c), most of the information in Γ is lost (all harmonics > 1 cycles/pixel are cut in the blue curve) while some low frequency content of the intensity image (red curve), including in particular the aliased peak at 0.39 cycles/pixel, are still retrieved. These asymmetric losses level the ratio between Γ and $\mathcal{B}$ in favour of $\mathcal{B}$, making the aliased peak at 0.39 cycles/pixel in the blue curve (due to $\mathcal{B}$) a bit more visible relative to this at 0.61 cycles/pixel (due to Γ). More details are provided section 1 of the supplementary document.

Funding. D.F. acknowledges financial support from the Royal Academy of Engineering Chair in Emerging Technology, UK Engineering and Physical Sciences Research Council (grants EP/T00097X/1 and EP/R030081/1) and from the European Union's Horizon 2020 research and innovation programme under grant agreement No 801060. H.D. acknowledges funding from the European Union's Horizon 2020 research and innovation programme under the Marie Skłodowska-Curie grant agreement No. 840958.

Contributions. H.D conceived the original idea, designed and performed experiments, analysed the data and prepared the manuscript. P.C. and H.D. performed the simulations. M.R. and J.F. contributed to developing the quantum illumination protocol with the EMCCD camera. J.Z and E.C. contributed to developing the quantum illumination protocol with the SPAD camera. A.L. and B.N. contributed to developing the entanglement-enabled quantum holography protocol. All authors contributed to the manuscript. D.F. supervised the project.

Competing interests. The authors declare no competing interests.

Data availability. All data that support the plots within this paper and other findings of this study are available from the corresponding author upon reasonable request.

Supplementary document

I. DETAILS ON THE JOINT PROBABILITY DISTRIBUTION (JPD) MEASUREMENT

This section provides more details about the measurement of the spatially resolved JPD of photon pairs using a Electron Multiplied Charge Coupled Device (EMCCD) or single-photon avalanche diode (SPAD) camera. Further theoretical details can be found in [27], [5] and [26].

A. JPD measurement.

EMCCD ans SPAD cameras can be used to reconstruct the (a) intensity distribution $I(\mathbf{r})$ and (b) the spatial joint probability distribution $\Gamma(\mathbf{r_1}, \mathbf{r_2})$ of photon pairs, where $\mathbf{r}$, $\mathbf{r_1}$ and $\mathbf{r_2}$ are positions of pixels. To do that, the camera first acquires a set of $N+1$ frames $\{I_l\}_{l\in[\![1,N+1]\!]}$ using a fixed exposure time and without using a threshold in the case of EMCCD camera. Then:

(a) The intensity image is reconstructed by averaging over all the frames:

$$I(\mathbf{r}) = \frac{1}{N}\sum_{l=1}^{N} I_l(\mathbf{r}) \tag{5}$$

(b) The JPD is reconstructed by performing the following substation:

$$\Gamma(\mathbf{r_1}, \mathbf{r_2}) = \frac{1}{N}\sum_{l=1}^{N} I_l(\mathbf{r_1})I_l(\mathbf{r_2}) - \frac{1}{N}\sum_{l=1}^{N} I_l(\mathbf{r_1})I_{l+1}(\mathbf{r_2}) \tag{6}$$

Under illumination by the photon pairs, intensity correlations in the left term of Equation 6 originate from detections of both real coincidences (two photons from the same entangled pair) and accidental coincidences (two photons from two different entangled pairs), while intensity correlations in the second term originate only from photons from different entangled pairs (accidental coincidence) because there is zero probability for two photons from the same entangled pair to be detected in two successive images. A subtraction between these two terms leaves only genuine coincidences, that are proportional to the spatial JPD of the pairs.

B. Interpolation of some JPD values measured with an EMCCD camera.

Using an EMCCD camera, not all correlation values of the JPD can be measured using Equation 6, in particular those (a) at the same pixel i.e. $\Gamma(\mathbf{r}, \mathbf{r})$ and (b) and those between vertical neighbouring pixels i.e. $\Gamma(\mathbf{r}, \mathbf{r} \pm \mathbf{e_y})$ (where $\mathbf{e_y}$ is the unit pixel vector in transverse direction y):

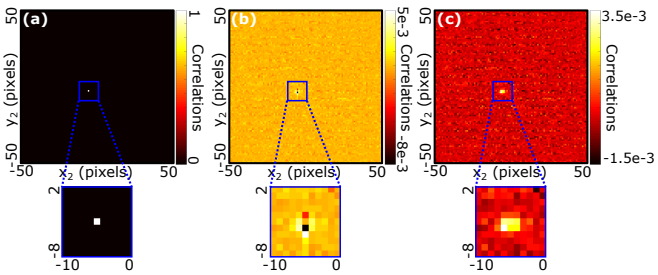

Figure 7. **Interpolation of JPD values when using EMCCD camera. (a)** Conditional image $\Gamma(\mathbf{r_1}, \mathbf{r_2})$ for a reference pixel $\mathbf{r_1} = (-5, 3)$ directly obtained from the JPD measured in the experiment described in Figure 1.a without interpolating the pixel values. **(b)** Same conditional image obtained after interpolating the diagonal values $\Gamma(\mathbf{r}, \mathbf{r})$ of the measured JPD. **(c)** Same conditional image obtained after interpolating all the values $\Gamma(\mathbf{r}, \mathbf{r} \pm k_y\mathbf{e_y})$ of the measured JPD, where k_y is an integer that correspond to an arbitrary number of vertical pixel above or bellow $\mathbf{r}$, and $\mathbf{e_y}$ is the unit vector pixel in the y-axis.

(a) As demonstrated in theory in [27], Equation 6 is not valid for $\mathbf{r_1} = \mathbf{r_2}$. For example, Figure 7.a shows a conditional image $\Gamma(\mathbf{r_1}, \mathbf{r_2})$ for a reference pixel $\mathbf{r_1} = (-5, 3)$ obtained from the JPD measured in the experiment described in Figure 1.a of the manuscript using Equation 6. In this image, we observe that the value at $\mathbf{r_2} = \mathbf{r_1}$ is more than 10^3 times brighter than the other images values, confirming that this value is wrong. In practice, this issue is solved by interpolating all the values in the diagonal $\Gamma(\mathbf{r}, \mathbf{r})$ using neighbouring correlation values on the same row: $[\Gamma(\mathbf{r}, \mathbf{r}+\mathbf{e_x})+\Gamma(\mathbf{r}, \mathbf{r}-\mathbf{e_x})]/2 \rightarrow \Gamma(\mathbf{r}, \mathbf{r})$ ($\mathbf{e_x}$ is the unit pixel vector in transverse direction x). Figure 7.b shows the conditional image $\Gamma(\mathbf{r_1}, \mathbf{r_2})$ for $\mathbf{r_1} = (-5, 3)$ obtained after interpolating the pixel value at $\mathbf{r_2} = \mathbf{r_1}$. More details in [5].

(b) However, we still observe in Figure 7.b the presence of artefacts in the values at positions $\mathbf{r_2} = \mathbf{r_1} \pm k_y\mathbf{e_y}$, where k_y is an integer that defines the position of a pixel above or bellow $\mathbf{r_1}$. These artefacts are due to cross-talk between pixels located on the same column of the EMCCD camera, originating from the so-called charge smearing effect [5]. In practice, these values are interpolated using neighbouring correlation values on the same row: $[\Gamma(\mathbf{r}, \mathbf{r} + \mathbf{e_x}) + \Gamma(\mathbf{r}, \mathbf{r} - \mathbf{e_x})]/2 \rightarrow \Gamma(\mathbf{r}, \mathbf{r})$ and $[\Gamma(\mathbf{r}, \mathbf{r} \pm k_y\mathbf{e_y} + \mathbf{e_x}) + \Gamma(\mathbf{r}, \mathbf{r} \pm k_y\mathbf{e_y} - \mathbf{e_x})]/2 \rightarrow \Gamma(\mathbf{r}, \mathbf{r} \pm k_y\mathbf{e_y})$. Figure 7.c shows the resulting conditional image $\Gamma(\mathbf{r_1}, \mathbf{r_2})$ for $\mathbf{r_1} = (-5, 3)$ after interpolating the pixel values.

C. Interpolation of some JPD values measured with an EMCCD camera.

Similar issues are encountered when measuring the JPD with a SPAD camera, as shown in Figure 3.d of the manuscript. (a) Equation 6 is not valid for $\mathbf{r_1} = \mathbf{r_2}$ and therefore cannot be used to measure the main diagonal $\Gamma(\mathbf{r}, \mathbf{r})$. (b) The presence of cross-talk between neighbouring pixels of the SPAD camera also corrupt the values in the 8 other diagonals $\Gamma(\mathbf{r}, \mathbf{r} \pm \mathbf{e_x} \pm \mathbf{e_y})$. In practice, this problem can be solved by setting all these values to 0 and using another configuration than a near-field illumination configuration to perform imaging. In Figure 3.d of the manuscript, we did that by using a far-field illumination so that the image information content is located in the anti-diagonal components of the JPD and not on its diagonals. More details in [26].

D. Residual term in the measured JPD using EMCCD camera.

The use of Equation 6 to measure the JPD with an EMCCD camera is not perfect and a residual background B is also retrieved: $\Gamma(\mathbf{r_1}, \mathbf{r_2}) + \mathcal{B}$. This problem is studied in [27]. This background term originates from the fluctuations of the EMCCD camera gain during the acquisition process, for example due to temperature drifts and variations in the high voltage clock amplitude. $\mathcal{B}$ is a complex term proportional to $\alpha I(\mathbf{r_1})I(\mathbf{r_2}) + \beta(I(\mathbf{r_1}) + I(\mathbf{r_2})) + \gamma$, where $I(\mathbf{r})$ is the intensity value at pixel $\mathbf{r}$, and α, β and γ are constant experimental parameters depending on the mean and variance values of the camera gain and electronic noise. In practice, $\mathcal{B}$ is often negligible compared to Γ and can be ignored in most experiments. However, because Γ and $\mathcal{B}$ do not have the same spatial frequency content, spatial filtering effects can create asymmetric losses and level these two terms in favor of $\mathcal{B}$. In particular, it is the case in Figure 2.c of the manuscript where spatial frequency contents are filtered asymmetrically by pixellation.

II. JPD PROJECTIONS IN A PIXELATED SPACE.

In the experiments shown in our work, the measured JPDs Γ takes the form of a 4-dimensional matrix containing $(M_Y \times M_X)^4$ elements, where $M_Y \times M_X$ corresponds the size of the illuminated region of the camera sensor. An element of the matrix is written $\Gamma(\mathbf{r_1}, \mathbf{r_2})$, where $\mathbf{r_1} = x_1\mathbf{e_x} + y_1\mathbf{e_y}$ and $\mathbf{r_2} = x_2\mathbf{e_x} + y_2\mathbf{e_y}$ are the spatial coordinates of two pixels. These coordinates are discrete: $x_i \in [1, M_X]$ and $y_i \in [1, M_Y]$ (where $i = 1$ or 2). In our work, the information content of Γ is analysed using two types of projections:

1. In theory, the sum-coordinate projection is defined as:

$$P_+(\mathbf{r}^+) = \int \Gamma(\mathbf{r}, \mathbf{r}^+ - \mathbf{r}) d\mathbf{r}. \tag{7}$$

In practice, it is calculated using the discrete space formula:

$$P_+(\mathbf{r}^+) = \sum_{x=1}^{M_X} \sum_{y=1}^{M_Y} \Gamma(\mathbf{r}, \mathbf{r}^+ - \mathbf{r}). \tag{8}$$

where $\mathbf{r} = x\mathbf{e_x} + y\mathbf{e_y}$. It represents the probability of detecting pairs of photons generated in all symmetric directions relative to the position $\mathbf{r}^+ = x^+\mathbf{e_x} + y^+\mathbf{e_y}$.

2. In theory, the sum-coordinate projection is defined as:

$$P_-(\mathbf{r}^-) = \int \Gamma(\mathbf{r}, \mathbf{r}^+ + \mathbf{r}) d\mathbf{r}. \tag{9}$$

In practice, it is calculated using the discrete space formula:

$$P_-(\mathbf{r}^-) = \sum_{x=1}^{M_X} \sum_{y=1}^{M_Y} \Gamma(\mathbf{r}, \mathbf{r}^- + \mathbf{r}). \tag{10}$$

where $\mathbf{r} = x\mathbf{e_x} + y\mathbf{e_y}$. This represents the probability for two photons of a pair to be detected in coincidence between pairs of pixels separated by an oriented distance $\mathbf{r}^- = x^-\mathbf{e_x} + y^-\mathbf{e_y}$.

III. SIMULATIONS OF THE JPD PIXEL SUPER-RESOLUTION TECHNIQUE

A. Near-field illumination configuration.

Figure 8 shows a 1D simulation illustrating the principle of our technique when using a near-field illumination configuration. In such a simple imaging configuration, described in Figure 8.a, a thin type-I BBO crystal is illuminated by a collimated blue pump laser to produce spatially-entangled photon pairs. Crystal surface, object (grid-shape) and camera are positioned in the same optical plane. In this simulation, photon-pairs are considered to be strongly correlated in space [28]: $\Gamma(x_1, x_2) \approx |t(x_1)t(x_2)\delta(x_1 - x_2)|^2$, where δ is a Dirac delta function. Figure 8.b shows the JPD of photon-pairs measured without the object. The JPD is 2D-matrix because the imaging system is 1D. The intense diagonal visible in the JPD is a clear signature of the near-perfect position correlations between photon pairs. After inserting the object, the diagonal of the JPD becomes modulated by the object shape (Figure 8.c). Figure 8.d shows the JPD after pixellation. Figure 8.e shows the JPD sum-coordinate projection, obtained by summing correlation values along the anti-diagonals. This projection

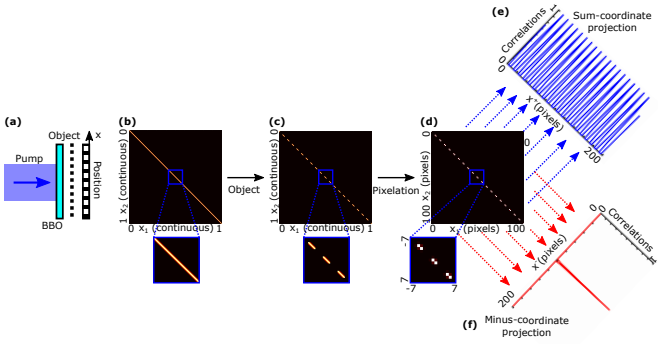

Figure 8. **Simple illustration of JPD pixel super-resolution using a near-filed illumination configuration.** **(a)** 1D scheme for imaging with spatially-entangled photon pairs using a near-field illumination configuration. Crystal surface, object and camera are positioned in the same optical plane. **(b)** JPD without object. **(c)** JPD with object. **(d)** JPD with object after pixellation. **(e)** Sum-coordinate projection of the JPD. **(f)** Minus-coordinate projection of the JPD.

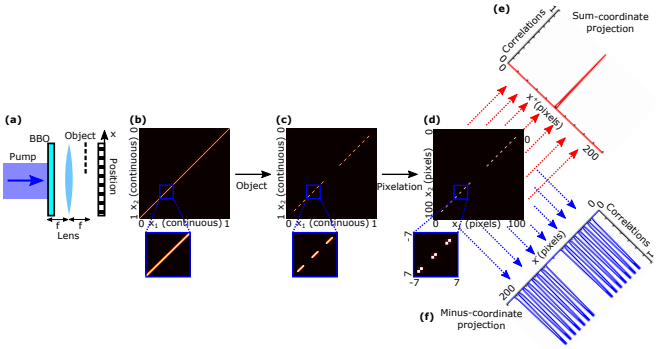

Figure 9. **Simple illustration of JPD pixel super-resolution using a far-filed illumination configuration.** **(a)** 1D scheme for imaging with spatially-entangled photon pairs using a far-field illumination configuration. Crystal surface is Fourier-imaged onto the object positioned in one half of the optical plane. Object is imaged on the camera. **(b)** JPD without object. **(c)** JPD with object. **(d)** JPD with object after pixellation. **(e)** Sum-coordinate projection of the JPD. **(f)** Minus-coordinate projection of the JPD.

enables to retrieve a pixel super-resolved image of the object i.e. $|t(x/2)|^2$. Figure 8.f shows the JPD minus-coordinate projection, obtained by summing correlation values along the diagonals. This projection shows an intensity correlation peak and is used in our work to select diagonals with the highest weights in the JPD filtering process (see section IV).

B. Far-field illumination configuration.

Figure 9 shows a 1D simulation illustrating the principle of our technique when using a far-field illumination configuration. In this simple configuration, described in Figure 9.a, a thin type-I BBO crystal is illuminated by a collimated blue pump laser to produce spatially-entangled photon pairs. The crystal surface is Fourier-imaged onto the object, that is imaged onto the camera. In this simulation, photon-pairs are considered to be strongly correlated [28]: $\Gamma(x_1, x_2) \approx |t(x_1)t(x_2)\delta(x_1 + x_2)|^2$ (where δ is a Dirac delta function). The object has a grid shape is positioned in only half of the optical plane (the other half is empty). Figure 9.b shows the JPD of photon-pairs measured without the object. The JPD is a 2D-matrix because the imaging system is 1D. The intense anti-diagonal visible in the JPD is a clear signature of the strong momentum correlations between photon-pairs. After inserting the object, we observe that each half of the JPD anti-diagonal become modulated by the object shape (Figure 9.d). Figure 8.d shows the JPD after pixellation. Figure 8.e shows the JPD sum-coordinate projection, obtained by summing correlation values along the anti-diagonals. This projection shows a intensity correlation peak and is used in our work to select anti-diagonals with the highest weights in the JPD filtering process (see section IV). Figure 8.f shows the JPD sum-coordinate projection, obtained by summing correlation values along the diagonals. This projection enables to retrieve a pixel super-resolved image proportional to $|t(x/2)||t(-x/2)|^2$. Because the object is positioned in only one half of the beam, the resulting image contains two copies of the pixel-super-resolved image.

C. 1D simulations of JPD pixel super-resolution.

1D simulations were performed by adapting the integral formalism of entangled photon pairs propagation provided in [28] to a matrix formalism computed with Matlab. Figure 10 shows simulated images of a grid-shape object (5 pixels period) obtained using a pixelated sensor and a near-field illumination configuration. Simulation parameters have been chosen to match those used in the experiment shown in Figure 1.a of the manuscript. Pixellation effect is well visible by eye when comparing the ground-truth object (Figure 10.a) to the intensity image (Figure 10.b). Figure 10.c shows the JPD sum-coordinate projection providing a better pixel resolution than the intensity image. Such a better resolution is confirmed when comparing the spatial frequency spectrum of both images in Figure 10.d. Indeed, the JPD projection spectrum (blue curve) contains harmonics at 0.6 cycles/pixel and 0.8 cycles/pixel, that are absent in the intensity image spectrum (red curve). These simulation results are in very good accordance with the experimental results obtained in Figure 1 of the manuscript. Figure 11 shows 1D simulations of spatial spectra calculated from images obtained with grid-shape objects of different periods. Simulation parameters have been chosen to be close to those used in the experimental results

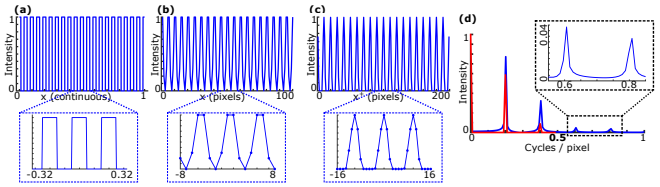

Figure 10. **1D simulation of JPD pixel-super-resolution. (a)** Ground-truth image of a grid-shape object with 5 pixels period (no pixellation). **(b)** Intensity image of the object acquired using a pixelated sensor and a near-field illumination configuration. **(c)** Sum-coordinate projection of the JPD acquired using a pixelated sensor and a near-field illumination configuration. **(d)** Spatial spectrum of the intensity (red curve) and sum-coordinate projection (blue curve) calculated by discrete Fourier transform. Simulation parameters have been chosen to match those used in the experiment shown in Figure 1.a of the manuscript.

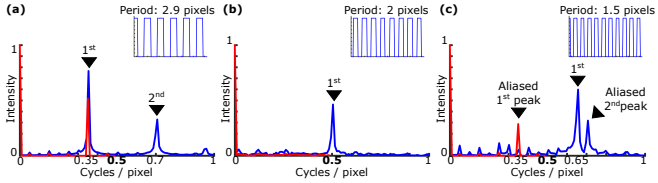

Figure 11. **1D simulations of spatial frequency spectra obtained from grid-shape objects with different periods.** Spatial frequency spectrum of intensity image (red curve) and sum-coordinate projection (blue curve) obtained by imaging grid-shape object with period of **(a)** $1/0.35 \approx 2.9$ pixels, **(b)** $1/0.5 = 2$ pixels and **(c)** $1/0.65 \approx 1.5$ pixels. Simulation parameters have been chosen to be close to those used in the experimental results shown in Figure 2 of the manuscript.

shown in Figure 2 of the manuscript. These spectra further confirm that the JPD sum-coordinate projection enables to retrieve spatial information that are not present in the intensity image, even in the case where the first harmonics has a higher frequency than the Nyquist frequency (Figure 11.c). These simulation results are in very good accordance with the experimental results obtained in Figure 2 of the manuscript. We however observe two small differences in Figure 11.c compared to Figure 2.c of the manuscript: (i) the absence of the residual first order aliased peak in the JPD projection curve and (ii) the presence of a second order aliased peak at 0.7 cycles/pixel. (i) is explained by the fact that the simulation do not use Equation 6 to produce the JPD and therefore does not contain the residual background term $\mathcal{B}$ at the origin of the first order aliased peak in Figure 2.c of the manuscript (see section I). (ii) is explained by the fact that no optical frequency cut-off is considered in the simulation, while it exists in the experiment. Such an optical cut-off causes a more rapid decrease of the higher harmonics in the experiment compared to the simulation, and therefore of their corresponding aliased peaks. The second order aliased peak is then too weak to be visible in the experimental spectrum shown in Figure 2.c, but is visible in the simulated spectrum shown in Figure 11.c.

IV. DETAILS ON JPD FILTERING

The JPD filtering method consists in setting to 0 values of the JPD that have a negligible weight (i.e. values close to zero) so that their associated noise do not contribute when performing the integration to calculate the JPD projection. To perform this selection efficiently, correlations values with the lowest weights are selected by groups. As explained in Methods, selecting these groups of correlation values require to differentiate the two cases of an object illuminated by photon pairs using (i) a near-field illumination configuration (Figures 1.a, 3.a and 5.a of the manuscript) and (ii) a far-field configuration (Figures 3.d and 4.a of the manuscript). In this section, we will describe step-by-step the filtering process in the case of the near-field illumination configuration. The same process can then be used in the far-field case by inverting the roles of P_- and P_+.

A. Image of a JPD diagonal average values.

First, the minus-coordinate projection of the JPD (noted P_-) is calculated using Equation 10. Each value $P_-(\mathbf{r}^-)$ is the sum of all the correlation values $\Gamma(\mathbf{r_1}, \mathbf{r_2} + \mathbf{r}^-)$ located on the diagonal defined by $\mathbf{r_1} - \mathbf{r_2} = \mathbf{r}^-$ and therefore provides a direct estimation of the corresponding diagonal average weight. Figure 12.a shows the minus-coordinate projection obtained using the JPD measured in the experiment of Figure 1.a of the manuscript (only the center area of 10×10 pixels is shown). We observe that only a small number of diagonals (pixels around the centrer) have significant weights, while all the others are almost zero.

B. Thresholding.

Second, a threshold T is applied to the minus-coordinate projection to select only the strongest values of P_- and their associated diagonals in the JPD. If $T = 0$ (no threshold), all JPD values are kept and the resulting JPD sum-coordinate projection is very noisy (Figure 12.e, same as Figure 6.a of the manuscript). If $T = 2\%$ of the image maximum value, only the diagonals associated with the values located in the area delimited by the blue line in Figure 12.d are kept, resulting into a sum-coordinate projection with less noise (Figure 12.f). For the higher threshold values of $T = 10\%$ (Figure 12.c) and $T = 50\%$ (Figure 12.d), the noise in the corresponding JPD sum-coordinate projection shown in Figure 12.g and h is further reduced. In this case, the best quality image is obtained using $T = 50\%$ (Figure 12.g), which cor-

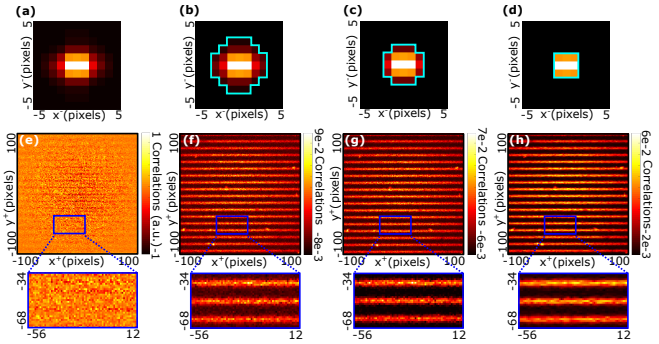

Figure 12. **JPD filtering.** **(a)** Minus-coordinate projection of the JPD measured in the experiment described in Figure 1.a of the manuscript before filtering (centred zoom of 30×30 pixels). **(b)** JPD minus-coordinate projection obtained after using a threshold $T = 2\%$ of the maximum. Values of the JPD diagonals associated with pixel values outside the blue line are set to zero. **(c)** JPD minus-coordinate projection obtained after using a threshold $T = 10\%$ of the maximum. **(d)** JPD minus-coordinate projection obtained after using a threshold $T = 10\%$ of the maximum. **(e)** JPD sum-coordinate projection obtained without filtering. **(f)** JPD sum-coordinate projection obtained after filtering with threshold $T = 2\%$ of the maximum. **(g)** JPD sum-coordinate projection obtained after filtering with a threshold $T = 10\%$ of the maximum. **(h)** JPD sum-coordinate projection obtained after filtering with a threshold $T = 50\%$ of the maximum.

responds to keeping only the correlations values of main JPD diagonal $\Gamma(\mathbf{r}, \mathbf{r})$ (i.e. center pixel of P_-) and those of the 8 other diagonals directly above and bellow i.e. $\Gamma(\mathbf{r}, \mathbf{r} \pm \mathbf{e_x})$, $\Gamma(\mathbf{r}, \mathbf{r} \pm \mathbf{e_y})$ and $\Gamma(\mathbf{r}, \mathbf{r} \pm \mathbf{e_x} \pm \mathbf{e_y})$ (direct-neighbour around the center pixel in P_-). A similar filtering thresholds was used also in all the other experiments shown in our work, resulting in keeping only the 9 diagonals (or anti-diagonals in far-field configuration) with highest weights. However, note that using the highest threshold level to keep only 9 diagonals/anti-diagonals is not necessarily the best solution. For example, if the correlation peak in the projection is asymmetric (e.g. due to optical aberrations in the imaging system), using a too high threshold can remove some diagonals in an asymmetric way and therefore create artefacts in the retrieved high-resolution image.

V. DETAILS ON ENTANGLEMENT-ENABLED QUANTUM HOLOGRAPHY

This section provides more details about the entangled-enabled quantum holography protocol used in Figure 4.a of the manuscript. This protocol has been introduced in [15].

A. Theory.

Assuming that photon-pairs are near-perfectly correlated in space [28], the vectorial two-photon wavefunction $\mathbf{\Psi}$ in the object/SLM plane simplifies as:

$$\mathbf{\Psi}(\mathbf{r_1}, \mathbf{r_2}) = \delta(\mathbf{r_1} + \mathbf{r_2})\big[t_6^H(\mathbf{r_1})t_6^H(\mathbf{r_2})\mathbf{e_H} + e^{i(\alpha(\mathbf{r_1})+\alpha(\mathbf{r_2}))}t_6^V(\mathbf{r_1})t_6^V(\mathbf{r_2})\mathbf{e_V}\big] \quad (11)$$

where t_6^H (resp. t_6^V) is the horizontal (resp. vertical) polarization component of the polarisation sensitive object t_6, $\mathbf{e_H}$ and $\mathbf{e_V}$ are the unit horizontal and vertical polarisation vectors, δ is the Dirac delta function and $\alpha(\mathbf{r})$ is the phase programmed at position $\mathbf{r}$ of the SLM. In the results shown in Figure 4 of the manuscript, t_6 is a birefringent object i.e. $t_6^H = |t_6|e^{\theta_H}$ and $t_6^V = |t_6|e^{\theta_V}$, where θ_H and θ_V are the horizontal and vertical polarization components of the object phase, respectively. As a result, after passing through the polariser at 45°, the JPD measured by the camera takes the form of :

$$\Gamma(\mathbf{r_1}, \mathbf{r_2}) = |t_6(\mathbf{r_1})t_6(\mathbf{r_2})\delta(\mathbf{r_1} + \mathbf{r_2})\big[1 + \cos\big(\Delta\theta(\mathbf{r_1}) + \Delta\theta(\mathbf{r_2}) - \alpha(\mathbf{r_1}) - \alpha(\mathbf{r_2})\big)\big]|^2 \quad (12)$$

where $\Delta\theta(\mathbf{r}) = \theta_H(\mathbf{r}) - \theta_V(\mathbf{r})$ is the object spatial phase that we are trying to retrieve.

B. Phase image retrieved using JPD anti-diagonals $\Gamma(\mathbf{r}, -\mathbf{r})$ (no pixel super-resolution).

To achieve quantum holography using the conventional protocol described in [15], only the anti-diagonal component of the JPD $\Gamma(\mathbf{r}, -\mathbf{r})$ needs to be considered. Taking into account that in our experiment (Figure 4.a of the manuscript) the object t_6 and the SLM are positioned on each halves of the optical plane (i.e. $t_6(x < 0, y) = 1$ and $\alpha(x > 0, y) = 0$), the JPD diagonal measured by the camera then simplifies as:

$$\Gamma(\mathbf{r}, -\mathbf{r}) = |t_6(\mathbf{r})|^2 \left[1 + \cos(\Delta\theta(-\mathbf{r}) - \alpha(\mathbf{r}))\right]^2 \quad (13)$$
$$\text{, for all } \mathbf{r} = (x > 0, y)$$

In the holographic reconstruction process, four JPD anti-diagonals (noted $\Gamma^\alpha(\mathbf{r}, -\mathbf{r})$) are measured for four different uniform phase shifts $\alpha(\mathbf{r}) \in \{0, \pi/2, \pi, 3\pi/2\}$ programmed on the SLM. Figures 13.c-f show the four anti-diagonal images measured at each phase value. The spatial phase $\Delta\theta(\mathbf{r})$ shown in Figure 13.k (and also in Figure 4.b of the manuscript) is then reconstructed from these four JPD anti-diagonals using the formula: $\arg[\Gamma^0(\mathbf{r}, -\mathbf{r}) - \Gamma^\pi(\mathbf{r}, -\mathbf{r}) + i(\Gamma^{\pi/2}(\mathbf{r}, -\mathbf{r}) - \Gamma^{3\pi/2}(\mathbf{r}, -\mathbf{r}))] = \Delta\theta(\mathbf{r})$. In practice, note also that a static and non-uniform phase distortion term (noted $\Phi_0(\mathbf{r})$) is also present in Equation 13, originating from the photon generation process [40]. This term is not shown here for clarify because it is directly compensated in the experiment by superimposing a correction phase pattern $-\Phi_0(\mathbf{r})$ to all the uniform phase α programmed

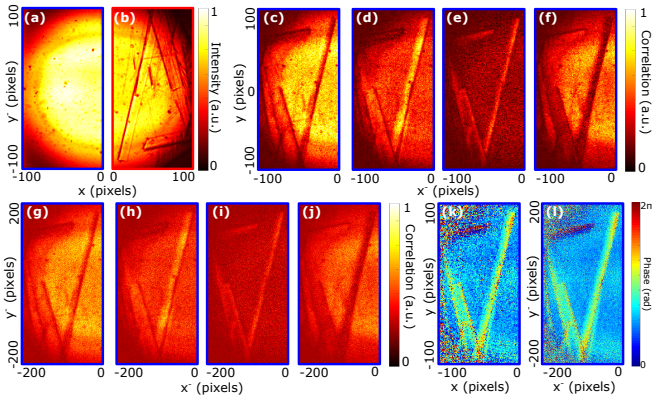

Figure 13. **Pixel super-resolution in entanglement-enabled quantum holography.** **(a)** and **(b)**, Intensity images measured on each half of the camera. **c-f**, JPD anti-diagonals $\Gamma^{\alpha}(\mathbf{r},-\mathbf{r})$ measured for $\alpha=0$ (c), $\alpha=\pi/2$ (d), $\alpha=\pi$ (e) and $\alpha=3\pi/2$ (f). **(g-j)**, JPD minus-coordinate projections $P_{-}^{\alpha}(\mathbf{r}^{-})$ measured for $\alpha=0$ (g), $\alpha=\pi/2$ (h), $\alpha=\pi$ (i) and $\alpha=3\pi/2$ (j). **(k)** Phase image retrieved using the anti-diagonal images (same as Figure 4.c of the manuscript). **(l)** Phase image retrieved using the minus-coordinate projections (same as Figure 4.d of the manuscript).

on the SLM (see [15] for more details about the phase correction).

C. Phase image retrieved using JPD minus-coordinate projections $P_{-}(\mathbf{r}^{-})$ (with pixel super-resolution).

To use our pixel super-resolution approach, the minus-coordinate projections (noted P_{-}^{α}) of the JPD is now considered instead of the anti-diagonal. Taking into account that in our experiment (Figure 4.a of the manuscript) the object t_6 and the SLM are positioned on each halves of the optical plane (i.e. $t_6(x<0,y)=1$ and $\alpha(x>0,y)=0$), the JPD minus-coordinate is calculated from Equation 12 and simplifies as:

$$P_{-}(\mathbf{r}^{-}) = |t_6(\mathbf{r}^{-}/2)|^2\big[1+\cos(\Delta\theta(-\mathbf{r}^{-}/2) - \alpha(\mathbf{r}^{-}/2))\big]^2, \text{ for all } \mathbf{r}=(x>0,y) \tag{14}$$

In the holographic reconstruction process, four JPD minus-coordinate projections (noted $P_{-}^{\alpha}(\mathbf{r}^{-})$) are measured for four different uniform phase shifts $\alpha(\mathbf{r}) \in \{0,\pi/2,\pi,3\pi/2\}$ programmed on the SLM. Figures 13.g-j show the four minus-coordinate projections measured at each phase value. The spatial phase $\Delta\theta$ shown in Figure 13.l (and also in Figure 4.c of the manuscript) is finally reconstructed by combining the four JPD minus-coordination projections using the formula: $\arg[P_{-}^{0}(\mathbf{r}^{-}) - P_{-}^{\pi}(\mathbf{r}^{-}) + i(P_{-}^{\pi/2}(\mathbf{r}^{-}) - P_{-}^{3\pi/2}(\mathbf{r}^{-}))] = \Delta\theta(\mathbf{r}^{-}/2)$. The resulting phase image has a better spatial resolution than the one shown in Figure 13.k measured using the conventional entanglement-enabled quantum holographic process.

VI. DETAILS ON FULL-FIELD NOON STATE QUANTUM HOLOGRAPHY

The use of optical NOON-state (N=2) for holographic imaging has been demonstrated by Ono et al [6] using a raster-scanning approach. In our work, we extended it to full-field imaging using the experiment described in Figure 5.a.

A. Theory.

Assuming that photon-pairs are near-perfectly correlated in space [28], the vectorial two-photon wavefunction $\mathbf{\Psi}$ in the object plane of the experiment described in Figure 5.a can be written as:

$$\mathbf{\Psi}(\mathbf{r_1},\mathbf{r_2}) = \delta(\mathbf{r_1}-\mathbf{r_2})\big[t_7^H(\mathbf{r_1})t_7^H(\mathbf{r_2})\mathbf{e_H} + e^{i(\alpha(\mathbf{r_1})+\alpha(\mathbf{r_2}))}t_7^V(\mathbf{r_1})t_7^V(\mathbf{r_2})\mathbf{e_V}\big] \tag{15}$$

where t_7^H (resp. t_7^V) is the horizontal (resp. vertical) polarization component of the polarisation sensitive object t_7, $\mathbf{e_H}$ and $\mathbf{e_V}$ are the unit horizontal and vertical polarisation vectors, δ is the Dirac delta function and $\alpha(\mathbf{r})$ is the phase programmed at position $\mathbf{r}$ of the SLM. In the results shown in Figure 5 of the manuscript, t_7 is a birefringent phase object produced by using a second SLM i.e. $t_7^H = e^{\theta_H}$ and $t_7^V = e^{\theta_V}$, where θ_H and θ_V are the horizontal and vertical polarization components of the phase. As a result, after passing through the polariser at 45°, the JPD measured by the camera takes the form of :

$$\Gamma(\mathbf{r_1},\mathbf{r_2}) = \delta(\mathbf{r_1}-\mathbf{r_2})\big[1+\cos\big(\Delta\theta(\mathbf{r_1}) + \Delta\theta(\mathbf{r_2}) - \alpha(\mathbf{r_1}) - \alpha(\mathbf{r_2})\big)\big]^2 \tag{16}$$

where $\Delta\theta(\mathbf{r}) = \theta_H(\mathbf{r}) - \theta_V(\mathbf{r})$ is the object spatial phase that we are trying to retrieve.

B. Double-phase effect in NOON-state holography (N=2).

In the experimental configuration shown in Figure 5.a of the manuscript, photon-pairs accumulate twice the phase of the object when passing through it at a given spatial position. In practice, this double-phase effect is precisely what provides this protocol a better phase sensitivity compared to classical holography, as already demonstrated in previous works using raster-scanning configurations [6, 7]. A simple way to visualise it is to measure JPD minus-coordinate projections (noted P_{-}^{α}) for different uniform phase pattern α programmed on the SLM with no object in the setup. In this case, P_{-}^{α} can

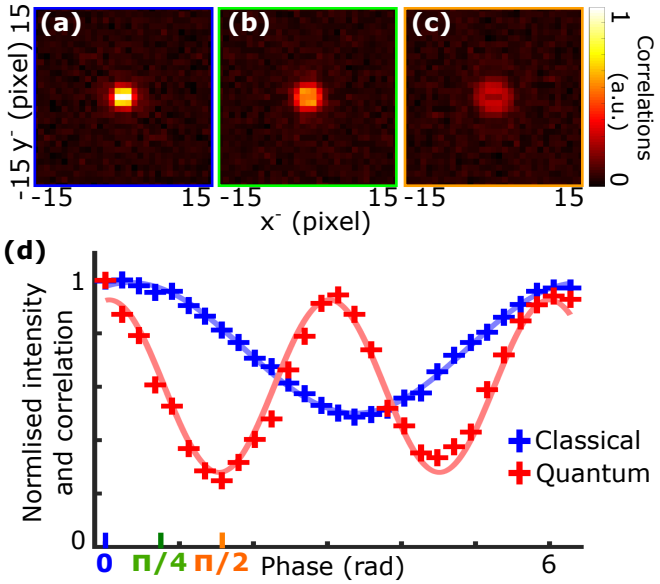

Figure 14. **Double-phase effect. (a - c)** JPD minus-coordinate projections measured using the experiment described in Figure 5.a of the manuscript with no object for different uniform phase values programmed on the SLM (a) $\alpha = 0$, (b) $\alpha = \pi/4$ and (c) $\alpha = \pi/2$ (only central areas of 30×30 pixels are shown). **(d)** JPD minus-coordinate correlation peak values (red curve) and average intensity values measured with an equivalent classical holography setup (blue curve) are represented for different $\alpha \in [0, 2\pi]$. The equivalent classical holography setup is described in section VI E.

be calculated from Equation 16 and takes the following theoretical form:

$$P_{-}(\mathbf{r}^{-}) = \left|1 + \cos\left(2\alpha\right)\right|^{2} \delta(\mathbf{r}^{-}) \tag{17}$$

where the double-phase effect is captured by the presence of the factor of 2 next to the SLM phase coefficient α. Figures 14.a-c show JPD minus-coordinate projections measured for different values of phases (a) $\alpha = 0$, (b) $\alpha = \pi/4$ and (c) $\alpha = \pi/2$ using the experimental setup in Figure 5.a of the manuscript with no object. As predicted by Equation 17, correlation value at the center peak (i.e. peak at $\mathbf{r}^{-} = \mathbf{0}$) varies with the value of α. Figure 14.d shows correlation peak values for 29 values of $\alpha \in [0, 2\pi]$ (red curve). This curve confirms the sine shape with a period of 1/2 predicted in Equation 17. As a comparison, average intensity values are measured using an equivalent classical holography setup (see section VI E) for $\alpha \in [0, 2\pi]$ are measured (blue curve). This curve shows the classical sine shape curve with a period of 1 (blue curve). Note that the contrast of these sine shape curves are not unity because the horizontal and vertical polarization components of entangled photons and classical light beams were not perfectly balanced in our experiments.

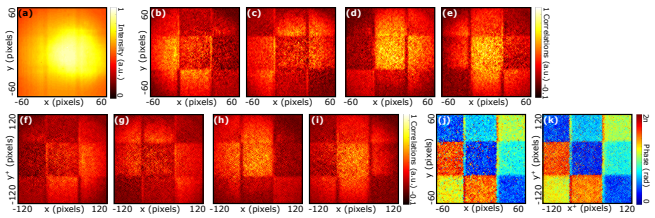

Figure 15. **NOON-state quantum holography using JPD diagonals and sum-coordinate projections. (a)** Constant intensity image acquired by the camera under photon-pairs illumination (not sensitive to the SLM phase). **b-e** JPD diagonals measured for four different phase values programmed on the SLM (b) $\alpha = 0$, (c) $\alpha = \pi/4$, (d) $\alpha = \pi/2$ and (e) $\alpha = 3\pi/4$. **f-i** JPD sum-coordinate projections measured for four different phase values programmed on the SLM (f) $\alpha = 0$, (g) $\alpha = \pi/4$, (h) $\alpha = \pi/2$ and (i) $\alpha = 3\pi/4$. **(j)** Phase image retrieved using the JPD diagonals. **(k)** Phase image retrieved using the JPD sum-coordinate projections (same as in Figure 5.c of the manuscript).

C. NOON-state quantum holography using the JPD diagonal $\Gamma(\mathbf{r}, \mathbf{r})$ (no pixel super-resolution).

In the presence of a birefringent phase object t_7 in the experimental setup, the JPD minus-coordinate projection cannot be used to retrieve its phase component $\Delta\theta(\mathbf{r})$. Instead, the JPD diagonal component $\Gamma(\mathbf{r}, \mathbf{r})$ is considered:

$$\Gamma(\mathbf{r}, \mathbf{r}) = \left|1 + \cos(2\Delta\theta(\mathbf{r}) - 2\alpha(\mathbf{r}))\right|^{2} \tag{18}$$

In the holographic reconstruction process, four JPD diagonals (noted $\Gamma^{\alpha}(\mathbf{r}, -\mathbf{r})$) are then measured for four different uniform phase shifts $\alpha(\mathbf{r}) \in \{0, \pi/4, \pi/2, 3\pi/4\}$ programmed on the SLM. Figures 15.b-e show the four diagonal images measured at each phase value. The spatial phase $2\Delta\theta(\mathbf{r})$ shown in Figure 15.j is finally reconstructed by combining these four diagonal images using the formula: $\arg[\Gamma^{0}(\mathbf{r}, \mathbf{r}) - \Gamma^{\pi/2}(\mathbf{r}, \mathbf{r}) + i(\Gamma^{\pi/4}(\mathbf{r}, \mathbf{r}) - \Gamma^{3\pi/4}(\mathbf{r}, \mathbf{r}))] = 2\Delta\theta(\mathbf{r})$. Note that, as predicted by the theory, the reconstructed phase is twice this of the object (i.e. $2\Delta\theta(\mathbf{r})$) because of the double-phase effect.

D. NOON-state quantum holography using the JPD sum-coordinate projection P_{+} (with pixel super-resolution).

To use our pixel super-resolution approach, the sum-coordinate projections (noted P_{+}^{α}) of the JPD are now considered instead of the JPD diagonals. The JPD sum-coordinate projection is calculated using Equation 16:

$$P_{+}(\mathbf{r}^{-}) = \left|1 + \cos(\Delta\theta(2\mathbf{r}^{+}/2) - 2\alpha(\mathbf{r}^{+}/2))\right|^{2} \tag{19}$$

In the holographic reconstruction process, four JPD sum-coordinate projections (noted $P_{+}^{\alpha}(\mathbf{r}^{-})$) are measured for four different uniform phase shifts $\alpha(\mathbf{r}) \in$

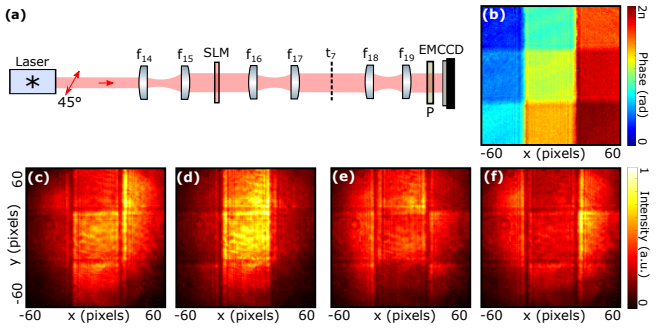

Figure 16. **Equivalent classical holography setup. (a)** Experimental setup used to perform classical holography. It is the same than this described in Figure 5.a of the manuscript after substituting the photon-pairs source by a collimated classical laser beam at 810nm and polarised at 45°. **(b)** Phase image retrieved by classical holography (same as Figure 5.d of the manuscript). **(c-f)** Intensity images measured for four different uniform phase values programmed on the SLM (c) $\alpha = 0$, (d) $\alpha = \pi/2$, (e) $\alpha = \pi$ and (f) $\alpha = 3\pi/2$.

$\{0, \pi/4, \pi/2, 3\pi/4\}$ programmed on the SLM. Figures 15.f-i show the four sum-coordinate projections measured at each phase value. The spatial phase $2\Delta\theta$ shown in Figure 15.l (and also in Figure 5.c of the manuscript) is finally reconstructed by combining these four JPD sum-coordinate projection using the formula: $\arg[P_+^0(\mathbf{r}^+) - P_+^{\pi/2}(\mathbf{r}^+) + i(P_+^{\pi/4}(\mathbf{r}^+) - P_+^{3\pi/4}(\mathbf{r}^+))] = 2\Delta\theta(\mathbf{r}^+/2)$. The resulting phase image has a better spatial resolution than the one shown in Figure 15.k measured using the JPD diagonal. Note that the reconstructed phase is also twice this of the object (i.e. $2\Delta\theta(\mathbf{r})$) because of the double-phase effect.

E. Equivalent classical holography setup.

The classical holography setup used to retrieve the phase in Figure 5.d of the manuscript is shown in Figure 16.a. It is the same setup than this described in Figure 5.a of the manuscript after substituting the photon-pairs source by a collimated classical laser beam at 810nm and polarised at 45°. In the holographic reconstruction process, four intensity images (noted I^α) are measured for four different uniform phase shifts $\alpha(\mathbf{r}) \in \{0, \pi/2, \pi, 3\pi/2\}$ programmed on the SLM. Figures 16.c-f show the four intensity images measured at each phase value. The spatial phase of the object $\Delta\theta$ (Figure 16.b and Figure 5.d of the manuscript) is finally reconstructed by combining these four intensity images using the formula: $\arg[I^0(\mathbf{r}) - I^\pi(\mathbf{r}) + i(I^{\pi/2}(\mathbf{r}) - I^{3\pi/2}(\mathbf{r}))] = \Delta\theta(\mathbf{r}/2)$.

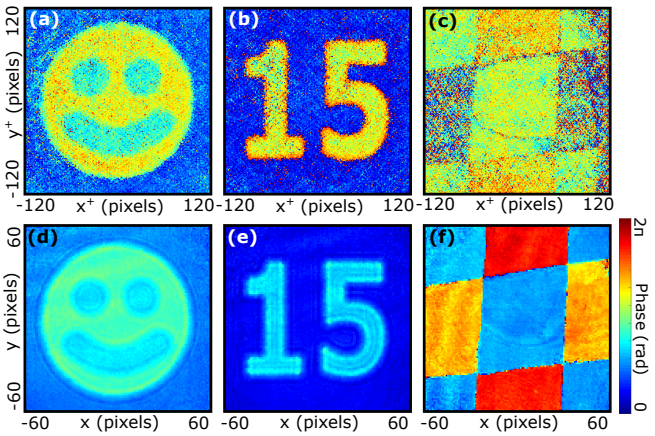

Figure 17. **Phase images of other artificial and real birefringent objects. (a-c)** Phase images of a (a) smiley face and (b) the number 15 created using another SLM retrieved by full-filed NOON-state quantum holography using the sum-coordinate projections. Phase image of (c) pieces of scotch tape forming a cross retrieved by full-filed NOON-state quantum holography (N=2). **(d-f)** Phase images of the same (d) smiley face, (e) the number 15 and (f) pieces of scotch tape retrieved by classical holography.

F. Other artificial and real birefringent phase objects measured using full-field NOON-state holography (N=2).

Figure 17 shows phase images of other artificial and real birefringent objects retreived by NOON-state quantum holography and classical holography. Note that the range of application of this full-field NOON-state holography technique can be extended to non-birefringent phase objects by using birefringent plates, as done in differential interference contrast microscopy [32].

VII. DIAGONAL AND ANTI-DIAGONAL IMAGES

Figure 18 shows diagonal and anti-diagonal images associated with the experiments shown in Figure 1.a, Figure 3.a and d, and Figure 5.a of the manuscript.

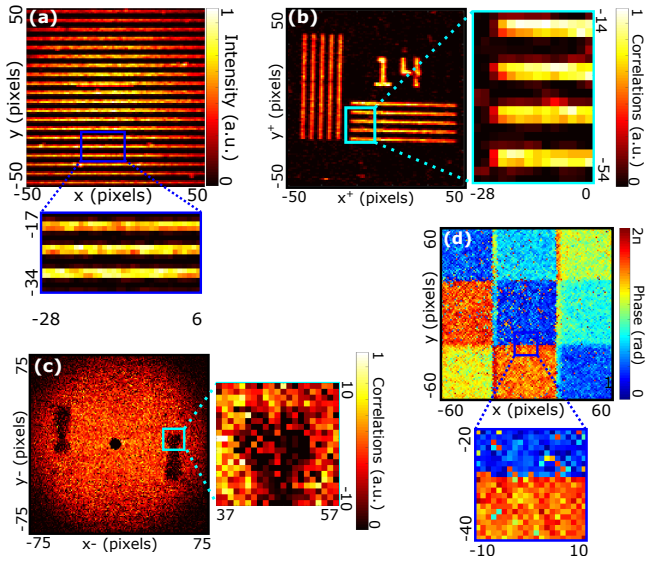

Figure 18. **Diagonal and anti-diagonal images. (a)** Diagonal image $\Gamma(\mathbf{r},\mathbf{r})$ measured using the experiment shown in Figure 1.a of the manuscript. **(b)** Diagonal image $\Gamma(\mathbf{r},\mathbf{r})$ measured using the experiment shown in Figure 3.a of the manuscript. **(c)** Anti-diagonal image $\Gamma(\mathbf{r},-\mathbf{r})$ measured using the experiment shown in Figure 3.d of the manuscript. **(d)** Diagonal image $\Gamma(\mathbf{r},\mathbf{r})$ measured using the experiment shown in Figure 5.a of the manuscript.

[1] W. Bishara, T.-W. Su, A. F. Coskun, and A. Ozcan, Optics Express **18**, 11181 (2010), publisher: Optical Society of America.

[2] W. Bishara, U. Sikora, O. Mudanyali, T.-W. Su, O. Yaglidere, S. Luckhart, and A. Ozcan, Lab on a Chip **11**, 1276 (2011).

[3] P.-A. Moreau, E. Toninelli, T. Gregory, and M. J. Padgett, Nature Reviews Physics **1**, 367 (2019).

[4] A. N. Boto, P. Kok, D. S. Abrams, S. L. Braunstein, C. P. Williams, and J. P. Dowling, Physical Review Letters **85**, 2733 (2000).

[5] M. Reichert, H. Defienne, and J. W. Fleischer, Scientific reports **8**, 7925 (2018).

[6] T. Ono, R. Okamoto, and S. Takeuchi, Nature communications **4**, 2426 (2013).

[7] Y. Israel, S. Rosen, and Y. Silberberg, Physical Review Letters **112**, 103604 (2014).

[8] G. Brida, M. Genovese, and I. R. Berchera, Nature Photonics **4**, 227 (2010).

[9] T. B. Pittman, Y. H. Shih, D. V. Strekalov, and A. V. Sergienko, Physical Review A **52**, R3429 (1995).

[10] R. S. Aspden, D. S. Tasca, R. W. Boyd, and M. J. Padgett, New Journal of Physics **15**, 073032 (2013).

[11] E. D. Lopaeva, I. Ruo Berchera, I. P. Degiovanni, S. Olivares, G. Brida, and M. Genovese, Physical Review Letters **110**, 153603 (2013).

[12] H. Defienne, M. Reichert, J. W. Fleischer, and D. Faccio, Science Advances **5**, eaax0307 (2019).

[13] T. Gregory, P.-A. Moreau, E. Toninelli, and M. J. Padgett, Science Advances **6**, eaay2652 (2020).

[14] F. Devaux, A. Mosset, F. Bassignot, and E. Lantz, Physical Review A **99**, 033854 (2019).

[15] H. Defienne, B. Ndagano, A. Lyons, and D. Faccio, Nature Physics **17**, 591 (2021).

[16] G. B. Lemos, V. Borish, G. D. Cole, S. Ramelow, R. Lapkiewicz, and A. Zeilinger, Nature **512**, 409 (2014).

[17] I. Kviatkovsky, H. M. Chrzanowski, E. G. Avery, H. Bartolomaeus, and S. Ramelow, Science Advances **6**, eabd0264 (2020), publisher: American Association for the Advancement of Science Section: Research Article.

[18] A. Vanselow, A. Vanselow, P. Kaufmann, I. Zorin, B. Heise, H. M. Chrzanowski, S. Ramelow, and S. Ramelow, Optica **7**, 1729 (2020), publisher: Optical Society of America.

[19] P.-A. Moreau, J. Mougin-Sisini, F. Devaux, and E. Lantz, Physical Review A **86**, 010101 (2012).

[20] M. P. Edgar, D. S. Tasca, F. Izdebski, R. E. Warburton, J. Leach, M. Agnew, G. S. Buller, R. W. Boyd, and M. J. Padgett, Nature Communications **3**, 984 (2012).

[21] R. Chrapkiewicz, W. Wasilewski, and K. Banaszek, Optics Letters **39**, 5090 (2014).

[22] M. Unternährer, B. Bessire, L. Gasparini, D. Stoppa, and A. Stefanov, Optics Express **24**, 28829 (2016).

[23] E. Toninelli, P.-A. Moreau, T. Gregory, A. Mihalyi, M. Edgar, N. Radwell, and M. Padgett, Optica **6**, 347 (2019).
[24] R. Chrapkiewicz, M. Jachura, K. Banaszek, and W. Wasilewski, Nature Photonics **10**, 576 (2016).
[25] D. Bronzi, F. Villa, S. Tisa, A. Tosi, F. Zappa, D. Durini, S. Weyers, and W. Brockherde, IEEE Journal of Selected Topics in Quantum Electronics **20**, 354 (2014).
[26] H. Defienne, J. Zhao, E. Charbon, and D. Faccio, Physical Review A **103**, 042608 (2021).
[27] H. Defienne, M. Reichert, and J. W. Fleischer, Physical review letters **120**, 203604 (2018).
[28] A. F. Abouraddy, B. E. Saleh, A. V. Sergienko, and M. C. Teich, JOSA B **19**, 1174 (2002).
[29] M. Reichert, H. Defienne, X. Sun, and J. W. Fleischer, Journal of Optics **19**, 044004 (2017).
[30] S. Farsiu, M. Robinson, M. Elad, and P. Milanfar, IEEE Transactions on Image Processing **13**, 1327 (2004), conference Name: IEEE Transactions on Image Processing.
[31] J. Schneeloch and J. C. Howell, Journal of Optics **18**, 053501 (2016).
[32] R. D. Allen and G. B. David, Zeitschrift fur wissenschaftliche Mikroskopie und mikroskopische Technik **69**, 193 (1969).
[33] R. A. Terborg, J. Pello, I. Mannelli, J. P. Torres, and V. Pruneri, Science Advances **2**, e1600077 (2016).
[34] W. Luo, Y. Zhang, A. Feizi, Z. Göröcs, and A. Ozcan, Light: Science & Applications **5**, e16060 (2016), number: 4 Publisher: Nature Publishing Group.
[35] W. Shi, J. Caballero, F. Huszar, J. Totz, A. P. Aitken, R. Bishop, D. Rueckert, and Z. Wang (2016) pp. 1874–1883.
[36] A. C. Ulku, C. Bruschini, I. M. Antolović, Y. Kuo, R. Ankri, S. Weiss, X. Michalet, and E. Charbon, IEEE Journal of Selected Topics in Quantum Electronics **25**, 1 (2019), conference Name: IEEE Journal of Selected Topics in Quantum Electronics.
[37] S. Farsiu, M. Elad, and P. Milanfar, in *Visual Communications and Image Processing 2006*, Vol. 6077 (International Society for Optics and Photonics, 2006) p. 607703.
[38] H. Takeda, S. Farsiu, and P. Milanfar, IEEE Transactions on Image Processing **16**, 349 (2007), conference Name: IEEE Transactions on Image Processing.
[39] I. Yamaguchi and T. Zhang, Optics Letters **22**, 1268 (1997).
[40] S. F. Hegazy and S. S. A. Obayya, JOSA B **32**, 445 (2015).